

# Chapter 1

## Theoretical Background

As previously stated, light can be confined below the diffraction limit by exploiting plasmons. Transferring energy from a diffraction-limited photonic field into collective oscillations of conduction electrons enhances the electric field on the surface of a metallic nanostructure with nanoscale localisation. It is through the understanding and application of this phenomenon that nano-optics and sub-wavelength confinement is made possible. This chapter deals firstly with a theoretical description of electromagnetic fields and the optical properties of metals. From this basis the concept of a plasmon can be introduced and the different kinds of plasmons defined, illustrating how they interact within different spatial regimes. Through this behaviour, the study of charge transfer in plasmonic systems, specifically quantum charge transport, is addressed. Finally, the plasmonics of metallic tips is discussed in preparation for the experiments described in later chapters studying plasmon interaction through each of the characteristic spatial regimes.

### 1.1 Plasmons

Plasmons are a direct solution of Maxwell's equations at the boundary between a dielectric and a metal. Despite existing on length scales from 100 nm down to around 1 nm, the high free electron density of metals mean energy levels still retain their characteristic continuous conduction bands and quantisation effects can be ignored.<sup>1</sup> Hence, classical theory is able to accurately describe physical phenomena until the characteristic length scale drops below  $\sim 0.5$  nm and a phenomenological approach using Maxwell's equations forms the basis of the mathematical description of plasmons.

---

<sup>1</sup>A higher density of states means that energy levels are more closely spaced, hence metals with a large free electron density appear to have an energy continuum as opposed to discrete energy bands or levels at room temperature.

### 1.1.1 Electromagnetic Waves

Maxwell's equations universally describe the classical, dynamical behaviour of electromagnetic (EM) waves, representing the foundations of electromagnetism. In their differential form they are given by,

$$\nabla \cdot \mathbf{E} = \frac{\rho_{\text{tot}}}{\epsilon\epsilon_0}, \quad (1.1\text{a})$$

$$\nabla \cdot \mathbf{B} = 0, \quad (1.1\text{b})$$

$$\nabla \times \mathbf{E} = -\frac{\partial \mathbf{B}}{\partial t}, \quad (1.1\text{c})$$

$$\nabla \times \mathbf{B} = \mu\mu_0 \left( \mathbf{J} + \epsilon\epsilon_0 \frac{\partial \mathbf{E}}{\partial t} \right), \quad (1.1\text{d})$$

where  $\mathbf{E}$  is the electric field,  $\mathbf{B}$  is the magnetic flux density,  $\epsilon_0$  is the permittivity of free space,  $\mu_0$  is the permeability of free space,  $\rho_{\text{tot}}$  is the (volume) charge density,  $\mathbf{J}$  is the current density and  $t$  is time. The variables  $\epsilon$  and  $\mu$  are the relative permittivity and permeability, respectively, and describe the electromagnetic properties of the medium in which the fields exist. The *electric displacement field*  $\mathbf{D}$  and the *magnetic field*  $\mathbf{H}$  can be introduced to include material dependencies and describe macroscopic fields, which are defined by,

$$\mathbf{D} = \epsilon_0 \mathbf{E} + \mathbf{P}, \quad (1.2\text{a})$$

$$\mathbf{H} = \frac{1}{\mu_0} \mathbf{B} + \mathbf{M}, \quad (1.2\text{b})$$

where  $\mathbf{P}$  is the polarisation (dipole moment per unit volume) and  $\mathbf{M}$  the magnetisation. Equations Eq. 1.1a and Eq. 1.1d can then be redefined as,

$$\nabla \cdot \mathbf{D} = \rho_{\text{ext}}, \quad (1.3\text{a})$$

$$\nabla \times \mathbf{H} = \mathbf{J}_{\text{ext}} + \frac{\partial \mathbf{D}}{\partial t}, \quad (1.3\text{b})$$

to describe macroscopic EM fields within media. The charge and current densities now refer to only the external contributions, related to the internal contributions via  $\rho_{\text{tot}} = \rho_{\text{ext}} + \rho_{\text{int}}$  and  $\mathbf{J}_{\text{tot}} = \mathbf{J}_{\text{ext}} + \mathbf{J}_{\text{int}}$ .

The displacement field arises due to polarisation of a material in response to an applied field and is related to the internal charge density by  $\nabla \cdot \mathbf{P} = \rho_{\text{int}}$ . Conservation of charge means that  $\nabla \cdot \mathbf{J} = \partial \rho / \partial t$ , which requires that  $\mathbf{J} = \partial \mathbf{P} / \partial t$  (a result also achievable by differentiating Eq. 1.2a). The final equation of importance is the relationship between the electric field and the current density, given by,

$$\mathbf{J} = \sigma \mathbf{E}, \quad (1.4)$$

where  $\sigma$  is the conductivity. These few relations are sufficient to understand the behaviour of electromagnetic waves in media.

Propagation of EM waves within a medium is governed by a wave equation relating both the spatial and temporal changes of a wave. Combining Eq. 1.1c and Eq. 1.1d leads to the general wave equation for EM waves in the time domain,

$$\nabla(\nabla \cdot \mathbf{E}) - \nabla^2 \mathbf{E} = -\varepsilon \varepsilon_0 \mu \mu_0 \frac{\partial^2 \mathbf{E}}{\partial t^2} - \mu \mu_0 \mathbf{J}, \quad (1.5)$$

describing the propagation of an EM wave in a given medium. In the absence of both charge and current Eq. 1.5 reduces to,

$$\nabla^2 \mathbf{E} = \varepsilon \varepsilon_0 \mu \mu_0 \frac{\partial^2 \mathbf{E}}{\partial t^2}, \quad (1.6)$$

describing a wave propagating in both space and time with a velocity  $v = 1/\sqrt{\varepsilon_0 \varepsilon \mu_0 \mu}$ . In free space ( $\varepsilon = \mu = 1$ ) this is the speed of light  $c = 1/\sqrt{\varepsilon_0 \mu_0}$ , with light slowed when in media to  $v = c/\tilde{n}$  by a factor  $\tilde{n} = \sqrt{\varepsilon \mu}$  known as the refractive index.

In general  $\varepsilon$  is a complex quantity,  $\varepsilon = \varepsilon_1 + i\varepsilon_2$ , and depends on the frequency of the EM wave,  $\omega$ . Plasmons are a phenomenon resulting from this frequency dependence in metallic materials. The relative permittivity is therefore denoted  $\varepsilon(\omega)$  and is referred to as the material's dielectric function from this point onwards. The concept of a plasmon can be identified through this function alone. Equations are therefore simplified by setting  $\mu = 1$  and removing any magnetic contributions. Since  $\varepsilon(\omega)$  is a complex parameter with components  $\varepsilon_1 + i\varepsilon_2$ , the complex refractive can be expressed as  $\tilde{n} = \sqrt{\varepsilon(\omega)} = n + i\kappa$ , where  $n$  is the real part causing refraction and  $\kappa$  is the loss coefficient determining absorption in the medium. The complex refractive index and the dielectric function are then related via  $\varepsilon_1 = n^2 - \kappa^2$  and  $\varepsilon_2 = 2n\kappa$ .

The dispersive properties of a material are found by solving Eq. 1.5 with  $\varepsilon = \varepsilon(\omega)$ , describing the behaviour of a wave propagating through a non-magnetic, dielectric medium. For a propagating EM wave with frequency  $\omega$  and wave vector  $\mathbf{k}$  in space  $\mathbf{r}$  of the form,

$$\mathbf{E} = \mathbf{E}_0 e^{i(\mathbf{k} \cdot \mathbf{r} - \omega t)}, \quad (1.7)$$

Eq. 1.5 can be expressed in the frequency (Fourier) domain as,

$$\mathbf{k}(\mathbf{k} \cdot \mathbf{E}) - k^2 \mathbf{E} = -\varepsilon(\mathbf{k}, \omega) \frac{\omega^2}{c^2} \mathbf{E}, \quad (1.8)$$

where  $k = |\mathbf{k}|$  is the magnitude of the wavevector. The variable  $k_0 = \omega/c$  is sometimes used in Eq. 1.8 when all quantities considered are wave vectors. From this equation the propagation behaviour of EM waves in media can be described.

Solutions to Eq. 1.8 depend on the orientation of the wavevector with the field. Transverse

wave solutions ( $\mathbf{k} \cdot \mathbf{E} = 0$ ) yield the dispersion relation for light,

$$k = \sqrt{\varepsilon(\mathbf{k}, \omega)} \frac{\omega}{c} = \tilde{n} k_0. \quad (1.9)$$

Inserting this into Eq. 1.7 gives a general solution for light propagating through a dielectric medium,

$$\mathbf{E} = \mathbf{E}_0 \exp(-\kappa k_0 r) \exp\left[i\omega\left(\frac{n}{c}r - t\right)\right]. \quad (1.10)$$

The real component of the refractive index  $n$  slows the wave whereas the imaginary component corresponds to an exponential decay with characteristic length  $1/\kappa$ , representing loss within a medium.

Longitudinal wave solutions ( $\mathbf{k} \cdot \mathbf{E} = k|\mathbf{E}|$ ) result in  $\sqrt{\varepsilon(\mathbf{k}, \omega)}\omega/c = 0$ , hence solutions only exists for  $\varepsilon(\mathbf{k}, \omega) = 0$ . Both these conditions are important when describing plasmons in the bulk of a metal (only longitudinal plasmons are supported) and on the surface (both transverse and longitudinal plasmons supported).

Lastly, it should be noted that if the material dielectric properties in  $\varepsilon$  are linear then  $\mathbf{D}$  can be expressed in Fourier space as,

$$\mathbf{D}(\mathbf{k}, \omega) = \varepsilon_0 \varepsilon(\mathbf{k}, \omega) \mathbf{E}(\mathbf{k}, \omega). \quad (1.11)$$

Combining Eq. 1.11 with the differential of Eq. 1.2a, Eq. 1.4 and Eq. 1.7<sup>2</sup> yields a relation between a material's conductivity and it's dielectric function,

$$\varepsilon(\mathbf{k}, \omega) = 1 + \frac{i\sigma(\mathbf{k}, \omega)}{\varepsilon_0 \omega}. \quad (1.12)$$

Both quantities are able to describe the same physics from a different perspective.<sup>3</sup> Since  $\text{Re}[\varepsilon]$  is related to both  $\text{Im}[\sigma]$  and  $\text{Re}[\tilde{n}]$ ,  $\text{Re}[\sigma]$  must therefore be related to  $\kappa = \text{Im}[\tilde{n}]$  and the attenuation of waves inside media. A large conductivity in a material therefore corresponds to large transmission losses with decay attributed to the energy needed to move electrons at the surface of the material. Furthermore, the relation between  $\varepsilon(\omega)$  and  $\sigma$  becomes important when considering points of conductance in a plasmonic system and that plasmons exist as an oscillating current.

Using the framework outlined so far the optical properties of metals can be deduced along with the existence of plasmons. The discussion begins with the Drude model for the optical response of metals [1], which is used to first predict the behaviour of plasmons. From there the distinction can be made between plasmons within the volume of a metal and those confined

<sup>2</sup> $\partial/\partial t \rightarrow -i\omega$  and  $\mathbf{J} = \dot{\mathbf{D}} - \varepsilon_0 \dot{\mathbf{E}} = \varepsilon_0 \dot{\mathbf{E}}(\varepsilon - 1) = \sigma \mathbf{E}$

<sup>3</sup>Choice of which variable to use is a matter of convenience and tradition. Either can be used to equally describe the electromagnetic response of a material. The conductivity is typically used to describe lower frequency phenomena while the dielectric function is used at higher frequencies.

to the surface, which are of most interest in plasmonics.

### 1.1.2 Bulk Plasmons and the Optical Properties of Metals

Before studying the concept of a surface plasmon it is important to understand the optical properties of metals as bulk materials. The optical properties of a metal are dominated by the response of nearly-free electrons delocalised from the positive nuclei background. When light is incident on a metal, nearly free electrons at the surface respond to the field and are displaced in the opposite direction (since  $\mathbf{F} = -e\mathbf{E}$ ). The field of the induced charge distribution cancels the electric field inside the metal. An EM wave impinging on a metal is internally screened, and therefore externally reflected,<sup>4</sup> through the displacement of free electrons inside the metal surface. The strong reflectance gives metals their shiny appearance. This behaviour originates from Eq. 1.12, where a high conductivity reduces the field penetration inside the metal. The exponential decay of the wave into the metal, shown in Eq. 1.10, is characterised by the skin depth  $\delta_m = c/2\omega\kappa$ , the point at which the field has decayed by 1/2e of its original value.<sup>5</sup> Light transmission through a metal becomes heavily attenuated once its thickness becomes greater than  $\delta_m$ . The small values of  $\delta_m$  exhibited by metals means that they fall within the *perfect conductor* approximation (zero internal field).

A metal starts to show a more “dielectric-like” behaviour when the frequency of incoming light is high enough that the inertia of the electrons means they cannot respond instantaneously, preventing screening and thus transmitting the incident light. Such effects begin to be seen in the visible region of the EM spectrum in the case of noble metals. Fields increasingly penetrate the metal up until ultraviolet (UV) photon energies, at which point most metals become transparent. This is known as the *ultraviolet transparency*.

Since the dominating cause of these effects stems almost exclusively from nearly free electrons, as opposed to bound electrons,<sup>6</sup> the optical properties of metals can be classically described by the Drude model [1]. This model describes the motion of a free electron gas in response to an applied field. The equation of motion for a single free electron in a time-varying applied field is given by,

$$m\ddot{\mathbf{x}}(t) + m\gamma\dot{\mathbf{x}}(t) = -e\mathbf{E}(t), \quad (1.13)$$

where  $m$  is its effective optical mass and  $\gamma = 1/\tau$  is the electron collision frequency, the inverse of the relaxation time,  $\tau$ . Using an effective optical mass as opposed to the actual electron mass incorporates band structure effects into the model. The electron collision frequency amounts to an effective coefficient of damping as in a mechanical oscillator. For a harmonic driving

<sup>4</sup>Light excites electrons into a higher energetic state leading to re-emission upon decaying back to the ground state, or from a different point of view, the prevention of light from entering the metal means the incident field must be reflected.

<sup>5</sup>The skin depth is defined using 1/2e rather than 1/e to consider power instead of field.

<sup>6</sup>Optical properties derived from bound electrons are described by a Lorentz oscillator model.

field, the induced oscillatory response of the free electrons induces a polarisation ( $\mathbf{P} = -nex$ , where  $n$  is the number density of electrons),

$$\mathbf{P}(t) = -\frac{ne^2}{m(\omega^2 + i\gamma\omega)} \mathbf{E}(t). \quad (1.14)$$

The resulting displacement field, obtained by substituting  $\mathbf{P}$  into Eq. 1.2a and using Eq. 1.11, defines the dielectric function of a metal,

$$\varepsilon(\omega) = 1 - \frac{\omega_p^2}{\omega^2 + i\gamma\omega}, \quad (1.15)$$

where  $\omega_p$  is the plasma frequency of the metal, given by,

$$\omega_p^2 = \frac{ne^2}{\varepsilon_0 m}. \quad (1.16)$$

The optical properties of a metal can be discerned from the real and imaginary components of  $\varepsilon(\omega)$ . The plasma frequency defines the point at which a metal transitions into a dielectric. For  $\omega < \omega_p$ ,  $\text{Re}[\varepsilon(\omega < \omega_p)] < 0$  and a free electron gas remains metallic in character, with electrons moving to oppose an incident field. Once  $\omega > \omega_p$  the free electron gas, limited by inertia, cannot respond fast enough to the field and the metal becomes dielectric in character. In real metals, interband transitions increase  $\text{Im}[\varepsilon(\omega)]$  and Eq. 1.15 has to be modified to account for interband absorption caused by bound electrons through the inclusion of a constant  $\varepsilon_\infty$ . The dielectric function then has the form,

$$\varepsilon(\omega) = \varepsilon_\infty - \frac{\omega_p^2}{\omega^2 + i\gamma\omega}. \quad (1.17)$$

A plot of Eq. 1.17 is shown in Figure 1.1, along with empirical data, illustrating both why noble metals exhibit high quality, visible spectrum (400–700 nm, 1.5–3 eV) plasmonics, as well as the failings of the Drude model. Noble metals have  $\text{Re}[\varepsilon(\omega)] < 0$  and small  $\text{Im}[\varepsilon(\omega)]$  in the visible region, hence behave very similarly to an ideal free electron gas. The Drude model fails at higher energies as interband transitions are not included in the basic model. These transitions increase the absorption ( $\propto \text{Im}[\varepsilon(\omega)]$ ) and are significant for  $\lambda < 500$  nm in Au and  $\lambda < 300$  nm in Ag. A measure of the quality of a metal can be determined from its quality factor  $Q = |\text{Re}[\varepsilon] / \text{Im}[\varepsilon]|$ . The high  $Q$  of noble metals in the visible regions means they can easily respond to an incident field and screen it, behaving metallically.

The plasma frequency  $\omega_p$  in  $\varepsilon(\omega)$  not only describes a metal-to-dielectric transition but also dictates the frequency of the collective longitudinal mode of oscillation. By substituting Eq. 1.15 in the zero damping limit into the dispersion relations for transverse and longitudinal

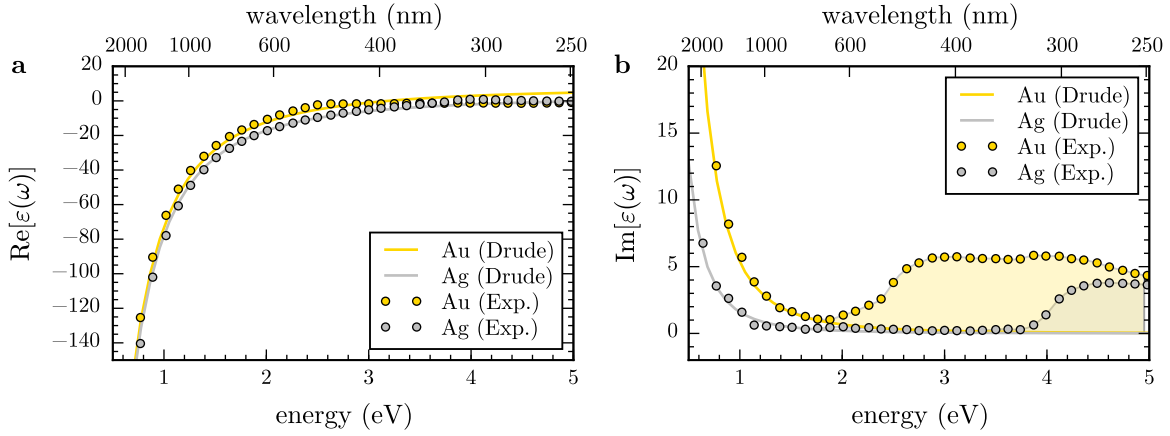


**Figure 1.1: Plot of the dielectric function, given by the Drude model, for Au and Ag compared with empirical data.**  $\epsilon(\omega)$  is calculated using Eq. 1.17. The plasma frequency is calculated using Eq. 1.16. The parameters of the curves are  $n = 5.90 \times 10^{28} \text{ m}^{-3}$ ,  $m = 9.11 \times 10^{-31} \text{ kg}$ ,  $\gamma = 1/\tau = 1/1 \times 10^{-14} \text{ s}$  and  $\epsilon_\infty = 8$  for Au and  $n = 5.86 \times 10^{28} \text{ m}^{-3}$ ,  $m = 9.11 \times 10^{-31} \text{ kg}$ ,  $\gamma = 1/\tau = 1/3 \times 10^{-15} \text{ s}$  and  $\epsilon_\infty = 3$  for Ag. Empirical data (Johnson and Christy, 1972 [2]) is shown for comparison to illustrate the importance of interband transitions. Differences between the Drude model (solid lines) and experimental results (circles) are caused by interband transitions not included in the basic Drude formalism.

waves it is clear that transverse waves are only supported if  $\omega > \omega_p$  with a dispersion  $\omega^2 = \omega_p^2 + k^2c^2$ . However, a collective longitudinal oscillation is allowed at  $\omega = \omega_p$  since  $\epsilon(\omega) = 0$  in the absence of damping. In this case the free electron gas is displaced from the ionic core background a distance  $u$  due to the applied field to form surface charge densities  $\sigma = \pm neu$ . The resulting depolarisation field<sup>7</sup> is  $E = neu/\epsilon_0$  and the motion of the free electrons is defined by,

$$nm\ddot{u} = -neE = -\frac{n^2e^2u}{\epsilon_0}. \quad (1.18)$$

Simplifying this relation leads to,

$$\ddot{u} + \omega_p^2 u = 0, \quad (1.19)$$

hence  $\omega_p$  is considered the natural frequency of the system and the electrons resonate when driven at  $\omega = \omega_p$ . This is known as the bulk or *volume plasmon*. Since this is a longitudinal oscillation, however, light cannot couple with it. For this reason, volume plasmons cannot be excited and measured by means of optical techniques but require other experimental methods (e.g. electron energy loss spectroscopy (EELS) [3]). Optical plasmonic phenomena must therefore be a result of a different kind of plasmon.

<sup>7</sup>Gauss' law  $\int \mathbf{E} \cdot d\mathbf{A} = Q/\epsilon_0 = \sigma A/\epsilon_0$ , hence  $E = \sigma/\epsilon_0$ . Alternatively  $D = 0 = \epsilon_0 \mathbf{E} + \mathbf{P}$  therefore  $\mathbf{E} = -\mathbf{P}/\epsilon_0 = -ne\mathbf{u}/\epsilon_0$ .

### 1.1.3 Surface Plasmons

Surface plasmons (SPs), unlike bulk plasmons, are collective oscillations of conduction electrons tightly confined to the surface of the metal and therefore not necessarily restricted by the diffraction limit. The maximum magnitude of the wavevector is set by  $k_0 = 2\pi/\lambda$  with individual components restricted by  $k = \sqrt{k_x^2 + k_y^2 + k_z^2}$ . Consider Eq. 1.9 in the form,

$$k_x^2 = \tilde{n}^2 k_0^2 - k_y^2 - k_z^2. \quad (1.20)$$

If a wave propagates freely in all three dimensions then it remains diffraction limited and the propagation constant  $k_x < \tilde{n}k_0$ . However if one or more of its wavevector components become imaginary ( $k_{y,z}^2 < 0$ ) then it becomes possible that  $k_x > \tilde{n}k_0$ . This behaviour can occur at an interface, where surface waves take on evanescent character in the  $z$ -direction whilst propagating in the  $xy$  plane.<sup>8</sup> By coupling light into surface waves the diffraction limit can be beaten. Waves of frequency  $\omega$  can acquire wavelengths many times smaller than their excitation wavelength. The SP is one such case of this phenomenon and occurs at metal-dielectric interfaces. Unlike in a bulk metal, electrons displaced by an applied field at the surface of a metal feel a restoring force due to the positive nuclei background. Transverse fields impinging on the metal surface at an angle are then able to manipulate the electron motion. SPs can therefore be excited by light as well as by the longitudinal waves needed to excite bulk plasmons, forming polariton quasiparticles under strong coupling with photons.<sup>9</sup> This optical excitation is known as the surface plasmon polariton (SPP) and, as a result of it being optically accessible, is one of the most commonly studied plasmonic phenomena.

### Surface Plasmon Polaritons

A SPP is a propagating transverse magnetic (TM) wave confined to the surface of a metal - the bound state between a photon and a SP. The TM nature of the wave indicates that **E** has a component traversing across the interface as shown in the diagram of a SPP in Figure 1.2. No such solution exists for transverse electric (TE) surfaces waves (i.e. a component of **H** passing through the interface).<sup>10</sup> While confined in two dimensions to the planar boundary between a metal and a dielectric, the SPP can either propagate or become stationary as a result of interference. The latter stationary form of the SPP is similar to the localised surface plasmons, described later.

The SPP itself is described through its dispersion. A TM wave propagating in the  $x$ -direction along a metal/dielectric interface has a spatial field profile in a space **x** given by

---

<sup>8</sup>Evanescent meaning imaginary  $k_z$  therefore exponentially decaying amplitude in the  $z$ -direction.

<sup>9</sup>Polaritons are the name given to quanta or quasiparticles of light-matter interactions. Strong coupling describes the point at which a quasiparticle is no longer distinguishable between its two constituent components.

<sup>10</sup>TE and TM are also known as *s*- and *p*-polarisations, respectively.

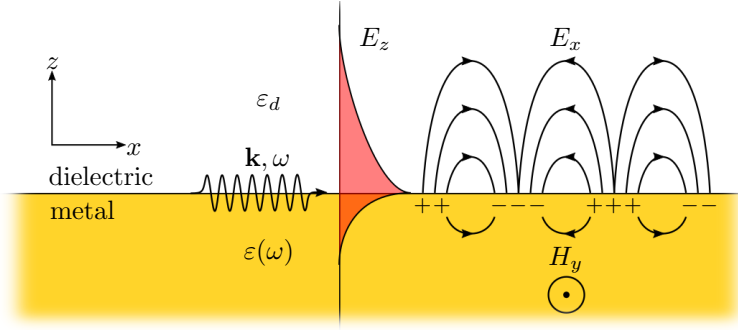


**Figure 1.2: Diagram of a surface plasmon polariton (SPP).** TM surface electron density waves (surface plasmons) couple with an evanescent wave originating from an EM wave to form a SPP. The SPP remains confined to the interface but can propagate across the surface.

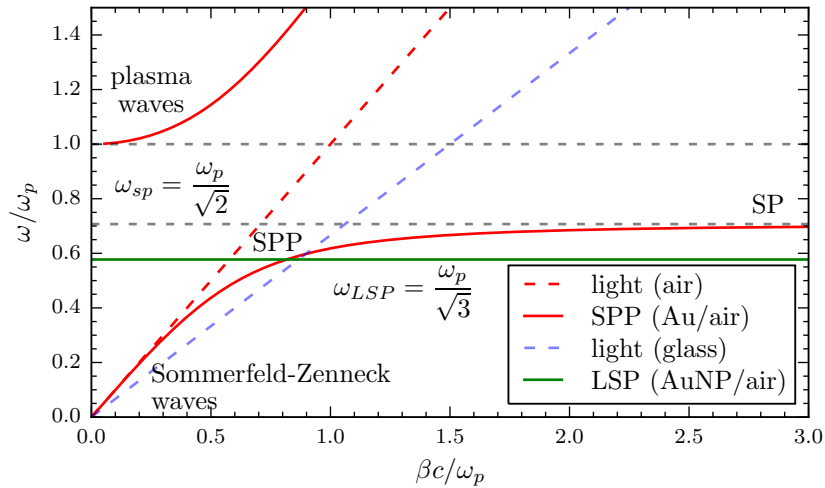


**Figure 1.3: Plasmon dispersion relations for the SPP and LSP.** The dashed lines indicate the dispersion of light in both glass and air (vacuum) along with the surface plasmon frequency. SPPs can be described as photon-like or plasmon-like depending on their point of excitation. SPPs excited with large  $k$  and  $\omega \approx \omega_{SPP}$  are considered plasmon-like while SPPs with low  $k$  are considered more photon-like. These have been known as Sommerfeld-Zenneck surface waves [4].

$\mathbf{E}(\mathbf{x}) = \mathbf{E}(z)e^{i\beta x}$  where  $\beta = k_x$  is the propagation constant. The magnetic field in this configuration is then  $\mathbf{H}(\mathbf{x}) = \mathbf{H}(y)e^{i\beta x}$ . Solving the wave equation across the metal-dielectric interface leads to the dispersion relation of a SPP, given by,

$$\beta = \frac{\omega}{c} \sqrt{\frac{\varepsilon_d \varepsilon(\omega)}{\varepsilon_d + \varepsilon(\omega)}}. \quad (1.21)$$

This dispersion is shown in Figure 1.3 along with the dispersion of light for both air and glass media.

From the dispersion curve it is clear that SPPs cannot couple with light within the same medium as their dispersion curves do not cross. However, light from within a higher refrac-

tive index medium such as glass can generate evanescent waves and excite SPPs on a nearby metal/air interface. This method of coupling photons with surface plasmons, depending on the specific prism arrangement, is known as the Kretschmann (prism-metal-dielectric) or Otto (prism-dielectric-metal) configuration [5, 6]. Since a diffraction grating may also impart momentum onto a photon ( $k_x \rightarrow k_x + n\pi$ ) a metallic grating can launch SPPs along a planar metal-dielectric interface. This phenomenon was first observed in 1902 by Wood, dubbed as Wood's anomaly [7], and only explained via surface waves many years later [8].

Closer inspection of the curve highlights one of the major features of a plasmon. While SPPs retain the frequency of the excitation field, their wavelength is considerably smaller than the diffraction-limited wavelength of light. Depending on where on the curve the SPP lies it can be considered to be either more photon-like or more plasmon-like. For small  $\beta \approx k_0$  the SPP is similar to light grazing the interface (Sommerfeld-Zenneck waves)<sup>11</sup> whereas SPPs with large  $k$  become more plasmon-like and their frequency saturates at the surface plasmon frequency,

$$\omega_{\text{SP}} = \frac{\omega_p}{\sqrt{1 + \varepsilon_d}}. \quad (1.22)$$

At this point the SPP can be considered electrostatic and becomes a SP. To some extent, SPs confined to a finite, continuous, non-planar surface, defining a metallic nanoparticle (MNP), can be considered to be the basis for localised surface plasmons (LSPs) or localised surface plasmon polaritons (LSPPs).

## Localised Surface Plasmons

LSPs are collective oscillations of conduction electrons confined within a fixed sub-wavelength spatial extent. These can occur on any nanoscale curved surface but the effects are strongest, and most well-documented, on the surface of a MNP. Free electrons are displaced from the nuclei in response to an applied field and form a surface charge distribution, polarising the particle. Coulomb interaction between the poles of the surface charge distribution results in a restoring force on electrons within the particle. This gives rise to a natural frequency of oscillation, leading to resonance when driven harmonically at the correct frequency. The particle geometry sets which multipolar surface charge distributions are supported, while its material properties and the dielectric properties of the surrounding medium set the restoring force. Each different multipolar charge distribution is therefore considered to be a unique LSP mode, identifiable by its optical resonance [9].

The simplest form of a LSP is the dipole resonance of a spherical MNP. Assuming the sphere radius  $a \ll \lambda$  (the wavelength of light), the particle is considered to be in the quasistatic regime, where electrons move instantaneously in response to the incident field and its phase

---

<sup>11</sup>Sommerfeld-Zenneck waves are surface waves that appear throughout mechanics and electromagnetism that are confined to the interface between two different mediums.

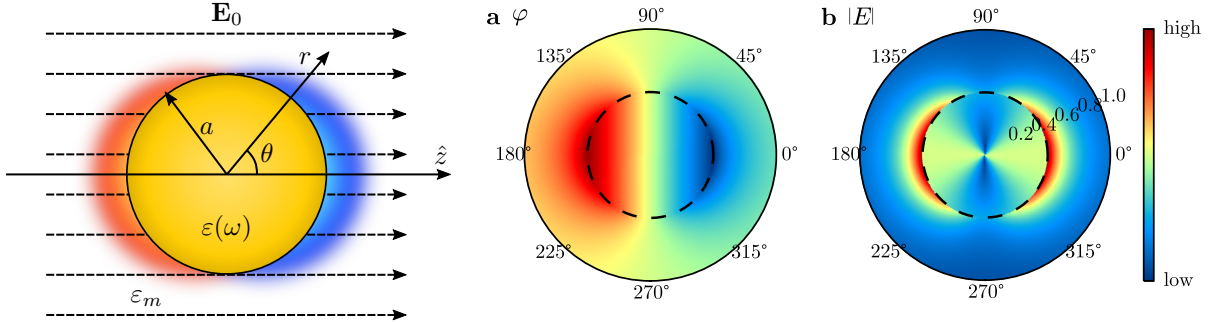


**Figure 1.4: A spherical metallic particle in an applied electric field.** The sphere is assumed to be in the quasistatic regime ( $a \ll \lambda$ ). The aura around the particle indicates the phase of the free electron oscillations in the plasmon. Calculations of (a) the potential and (b) the magnitude of the electric field for a spherical nanoparticle on resonance ( $\varepsilon(\omega) = -2\varepsilon_d$ ).

is ignored. Electrostatics, rather than electrodynamics, then becomes applicable to solve the problem. The electrostatic potential,  $\varphi$ , of the system is described by the Laplace equation,  $\nabla^2\varphi = 0$ , with a general solution in a spherical geometry of the form [10],

$$\varphi_{l,m_l}(r, \theta, \phi) = \sum_{l=0}^{l=\infty} \sum_{m_l=-l}^l [A_l r^l + B_l r^{-(l+1)}] P_l^m(\cos \theta) e^{im_l \phi}, \quad (1.23)$$

where  $l$  is the degree of spherical harmonic and  $m_l$  its projection,  $A_l$  and  $B_l$  are constants and  $P_l^m(\cos \theta)$  are associated Legendre polynomials. For a sphere of radius  $a$  and dielectric function  $\varepsilon(\omega)$  in a dielectric medium described by  $\varepsilon_d$  the solution is fixed by the boundary conditions  $\varphi_{\text{out}} \rightarrow -E_0 z$  as  $r \rightarrow \infty$  and  $\nabla \varphi_{\text{in}}(r)|_{r=a} = \nabla \varphi_{\text{out}}(r)|_{r=a}$ . This reduces to a solution [11],

$$\varphi = \begin{cases} -\frac{3\varepsilon_d}{\varepsilon(\omega) + 2\varepsilon_d} \mathbf{E}_0 \cdot \mathbf{r} & r \leq a \text{ (inside)}, \\ \left( -1 + \frac{\varepsilon(\omega) - \varepsilon_d}{\varepsilon(\omega) + 2\varepsilon_d} \frac{a^3}{r^3} \right) \mathbf{E}_0 \cdot \mathbf{r} & r > a \text{ (outside)}. \end{cases} \quad (1.24)$$

For a metal sphere the potential (plotted in Figure 1.4a) describes an induced dipolar surface charge distribution. The description is simplified by defining the dipole moment,

$$\mathbf{p} = \varepsilon_0 \varepsilon_d \alpha \mathbf{E}_0 = 4\pi \varepsilon_0 \varepsilon_d a^3 \frac{\varepsilon(\omega) - \varepsilon_d}{\varepsilon(\omega) + 2\varepsilon_d} \mathbf{E}_0, \quad (1.25)$$

where the polarisability,  $\alpha$ , incorporates the frequency dependent behaviour and is defined as,

$$\alpha(\omega) = 4\pi a^2 \frac{\varepsilon(\omega) - \varepsilon_d}{\varepsilon(\omega) + 2\varepsilon_d}. \quad (1.26)$$

The outside potential is then expressed as,

$$\varphi_{out} = -\mathbf{E}_0 \cdot \mathbf{r} + \frac{\mathbf{p} \cdot \mathbf{r}}{4\pi\epsilon_0\epsilon_d r^3}. \quad (1.27)$$

This is simply the potential of an induced dipole superimposed onto the incident field. The electric field inside and outside of the sphere, calculated using  $\mathbf{E} = -\nabla\varphi$  and given by,

$$\mathbf{E} = \begin{cases} \frac{3\epsilon_d}{\epsilon(\omega) + 2\epsilon_d} \mathbf{E}_0 & r \leq a \text{ (inside)}, \\ \mathbf{E}_0 + \frac{3\mathbf{n}(\mathbf{n} \cdot \mathbf{p}) - \mathbf{p}}{4\pi\epsilon_0\epsilon_d} \frac{1}{r^3} & r > a \text{ (outside)}, \end{cases} \quad (1.28)$$

where  $\mathbf{n} = \mathbf{r}/r$  is the radial unit vector, shows a similar phenomenon and is shown in Figure 1.4b.

Provided that the quasistatic approximation remains valid, the electrostatic result is simply multiplied with a harmonic time dependence to describe electrodynamic behaviour. An EM wave therefore induces a coherent, oscillating dipole moment  $\mathbf{p}e^{i\omega t} = \epsilon_0\epsilon_d\alpha\mathbf{E}_0e^{i\omega t}$ . The behaviour of electrons in the spherical MNP at optical frequencies, described using the dielectric function  $\epsilon(\omega)$ , is then simply incorporated into  $\alpha(\omega)$ . For a good metal  $\text{Re}[\epsilon(\omega)] < 0$  and the denominator in Eq. 1.26 undergoes resonance<sup>12</sup> at the Fröhlich condition when,

$$\text{Re}[\epsilon(\omega)] = -2\epsilon_d. \quad (1.29)$$

This corresponds to excitation of a collective oscillation of conduction electrons on the surface of the sphere - the dipolar LSP. Its magnitude in real metals is restricted by damping of the electron motion leading to a Lorentzian-shaped resonance band - the dipolar surface plasmon resonance (SPR). Its relationship with  $\epsilon_d$  means that the SPR can be tuned by varying the external dielectric medium. As seen in Eq. 1.28, the field from the induced dipole moment of the plasmon is superimposed onto the incident field leading to a resonant enhancement, both inside and outside the surface of the sphere. This is one of the fundamental properties of the plasmon, and one that is most exploited in sensing and sensor developments.

In the Drude model, with  $\epsilon(\omega)$  given by Eq. 1.17, the Fröhlich condition is satisfied when,

$$\omega_{LSP} = \frac{\omega_p}{\sqrt{1 + 2\epsilon_d}}, \quad (1.30)$$

which evaluates to  $\omega = \omega_p/\sqrt{3}$  for a MNP in vacuum. As can be seen in Figure 1.3, the flat dispersion of a LSP mode means it crosses the light line at a single point. Light of the correct frequency therefore readily couples with LSPs without the need for SPP momentum matching

---

<sup>12</sup> $\alpha \rightarrow -\infty$  when  $\epsilon(\omega) + 2\epsilon_d \rightarrow 0$

mechanisms. In general, the optical spectrum of a MNP can contain a number of multipolar plasmon modes for which the resonant frequencies are given by [12],

$$\omega_l = \omega_p \sqrt{\frac{l}{\varepsilon_d(l+1)+1}}, \quad (1.31)$$

where the degree of spherical harmonics  $l$  denotes the charge distribution of a specific mode ( $l = 1$  for dipole,  $l = 2$  for quadrupole, etc.). However, these modes only exist outside of the quasistatic regime in larger MNPs or more complex geometries. For nobles metals, such as Au and Ag, the fundamental  $l = 1$  mode occurs in the visible region of the EM spectrum ( $\lambda = 520$  nm for Au and  $\lambda = 360$  nm for Ag in vacuum or air [10], redshifted in the presence of other media [13]), leading to them often being the plasmonic metal of choice. Additionally, the polarisability changes with nanoparticle (NP) geometry due to differing restoring forces acting on the surface charge distribution. Changes from a spherical shaped NP therefore lead to tuning of the SPRs across the visible spectrum. This geometrical dependence is well known [14–16] and has been exploited in many applications over the past decade, e.g. infrared (IR) photothermal therapy [17–19].

The larger the separation between opposing poles of surface charge, the weaker the restoring force. A larger particle, or similarly an elongated particle (a nanoellipsoid or nanorod), will therefore have lower energy resonances. Simple changes can be made to the theoretical (quasistatic) model to account for an ellipsoidal geometry, and thus somewhat understand the geometrical dependencies incorporated into the polarisability. Insertion of a geometrical correction to the polarisability leads to the definition [10, 20],

$$\alpha_i(\omega) = 4\pi a_1 a_2 a_3 \frac{\varepsilon(\omega) - \varepsilon_d}{3\varepsilon_d + 3L_i(\varepsilon(\omega) - \varepsilon_d)}, \quad (1.32)$$

where  $i$  is the index of each anisotropic axis with a geometrical factor,

$$L_i = \frac{a_1 a_2 a_3}{2} \int_0^\infty \frac{dq}{(a_i^2 + q) \sqrt{(q + a_1^2)(q + a_2^2)(q + a_3^2)}}. \quad (1.33)$$

The resonance condition along each axis then becomes,

$$\text{Re}[\varepsilon(\omega)] = -\frac{1 - L_i}{L_i} \varepsilon_d. \quad (1.34)$$

By increasing the size of an axis, decreasing its associated geometrical factor, the resonance condition decreases from  $\varepsilon(\omega) = -2\varepsilon_d$ , redshifting the SPR. The more elongated the particle becomes, the larger the redshift until the restoring force is weakened to the point that each lowest-order antenna SPR no longer exists.

## Optical Observation of Surface Plasmon Resonances

Depending on the microscopic dipole moment of excited plasmons, their fields can be radiative and hence macroscopically observable. This depends on the geometry of the plasmons time-varying charge distribution. Antenna-like dipolar plasmons bear similarity with the Hertzian dipole, an infinitesimal oscillating current source which both absorbs and radiates EM waves. The relationship between the current,  $\mathbf{I}(t)$ , carried by the dipole of length  $d$  and the radiative electric field around it is given by [21],

$$\mathbf{E} = \frac{ik\mathbf{Id}\eta_o}{4\pi r} e^{-ikr} \left[ \hat{r} \left( \frac{1}{ikr} + \frac{1}{(ikr)^2} \right) 2 \cos \theta + \hat{\theta} \left( 1 + \frac{1}{ikr} + \frac{1}{(ikr)^2} \right) \sin \theta \right], \quad (1.35)$$

The radial behaviour of the electric field around an object can be split into three distinct regimes - the *near-field*, Fresnel regime and the *far-field* or Fraunhofer regime. At short distances the  $(kr)^{-2}$  term dominates to form the near-field but quickly falls off with increasing distance. The remaining  $(kr)^{-1}$  term defines the far-field. The Fresnel regime forms the intermediate stage between the two. The boundary between the near-field and the far-field is defined as the point at which  $kr = 1$  where  $r = \lambda/2\pi$  (hence why sub-wavelength optics deals with the near-field).

Plasmons similarly have the ability to both resonantly absorb and scatter incident fields. The absorbance and scattering cross sections determining interaction with a spherical MNP are given by [22],

$$\sigma_{\text{scat}} = \frac{k^4}{6\pi} |\alpha|^2 = \frac{8\pi}{3} k^4 a^6 \left| \frac{\varepsilon(\omega) - \varepsilon_d}{\varepsilon(\omega) + 2\varepsilon_d} \right|^2, \quad (1.36a)$$

$$\sigma_{\text{abs}} = k \text{Im}[\alpha] = 4\pi k a^3 \text{Im} \left[ \frac{\varepsilon(\omega) - \varepsilon_d}{\varepsilon(\omega) + 2\varepsilon_d} \right]. \quad (1.36b)$$

Since  $\sigma_{\text{scat}} \propto V^2$  and  $\sigma_{\text{abs}} \propto V$ , absorption dominates in smaller particles whilst larger particles scatter more strongly. The extinction cross section, commonly used in spectroscopy, can be calculated using  $\sigma_{\text{ext}} = \sigma_{\text{scat}} + \sigma_{\text{abs}}$ . The size of each cross-section, i.e. the spatial extent over which light interacts with the MNP, depends on  $\alpha$  and is increased on resonance. Hence, MNPs optically appear strongly coloured and much larger than they actually are.<sup>13</sup>

For example, when on resonance with the dipolar LSP, both cross sections are enhanced by the polarisability resonance from the geometrical particle size to the  $\mathcal{O}(500 \text{ nm})$  scattering size. The increased size of the cross-section is comparable to the wavelength of light, meaning LSPs efficiently couple with photons in the far-field. The LSP mediates energy transfer be-

---

<sup>13</sup>Consider that  $\sigma_{\text{scat}}$  for a AuNP is enhanced  $100\times$  on resonance, meaning its area cross-section is  $\sqrt{100/\pi} = 6\times$  wider than its radius, hence why a 50 nm AuNP looks like a 300 nm green sphere when imaged.

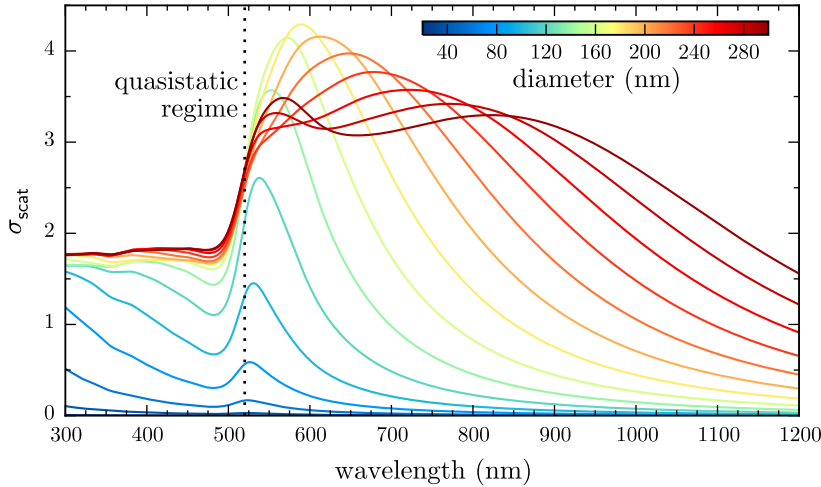


**Figure 1.5: Mie scattering cross-sections for AuNPs of increasing diameter.** The 520 nm resonance position of the dipolar LSP mode of a AuNP in the quasistatic approximation is indicated by the dotted line. The resonance stays at 520 nm until  $d > 80$  nm then redshifts. The emergence of higher order modes following a similar behaviour is seen once  $d > 100$  nm.

tween the near-field and the far-field and acts to match the electromagnetic modes of nanoscale absorbers/emitters, such as phonons (Raman) and radiative energy levels (quantum emitters, fluorescence), with those of a diffraction-limited photonic mode via an oscillating charge density [23]. A plasmonic NP is often therefore described as an *optical antenna* in a similar manner to a device that converts between radio waves and an electrical current is named a radio antenna [24, 25]. LSP modes which readily couple with the far-field are then sometimes referred to as *antenna modes* and become important when designing resonant structures for specific sensing applications.

Whilst the quasistatic approach is useful to first demonstrate the field enhancing capabilities of a MNP, the description breaks down once the size of the particle becomes closer to the excitation wavelength. Retardation effects result in phase differences between the incident field and the induced electron currents across the particle which strongly influence the radiated fields. At this point Mie theory (electrodynamics) [26] is required to describe the spectral response of spherical MNPs. Mie theory provides a more general description of the optical response of spherical MNPs. Using this approach the spectrum of a MNP can be decomposed into superimposed multipoles, arising from the existence of higher order LSP modes in larger MNPs with finite dipole moments. The spectral response of spherical AuNPs of varying sizes is shown in Figure 1.5, demonstrating the redshift and broadening of lower order modes with increasing particle size and the excitation of higher order modes.

To summarise, by utilising the particle material, geometry and polarisation anisotropy, its LSPs can be tuned across the entire UV–NIR spectrum to tailor to individual applications. However, even when exciting on resonance, a single particle can only provide a relatively

small field enhancement ( $|E/E_0| \sim \mathcal{O}(5 - 10)$ ). An alternative approach to exploiting LSPs is therefore to couple the fields of many plasmons together. Through coupling, the confined fields in nanometric-size gaps between MNPs can be enhanced by many more orders of magnitudes.

## 1.2 Plasmon Coupling

Both the resonant field enhancement and the confinement of a surface plasmon can be improved by bringing a second surface plasmon into close proximity. Similar to coupled harmonic oscillators and dipoles, plasmons couple together via Coulomb forces, forming normal modes of oscillation. The charge distribution of the resulting normal modes depends highly on the particle separation and is strongly confined to the dielectric space between metallic surfaces where charges strongly interact. These normal modes are therefore more generally known as *gap plasmons* and lead to tuneable plasmon resonances [27, 28] and significant increases in field enhancement, enabling single molecule spectroscopy [29, 30].

Coupled plasmons are a feature of many metallic nano-systems with closely spaced metal-dielectric interfaces, including metal-insulator-metal (MIM) and insulator-metal-insulator (IMI) waveguides [10, 31] and systems containing multiple MNPs [27, 28, 32–36] or nanoparticles-on-mirror (NPoM) [29, 37–41]. For the purposes of this work, discussion is restricted to the ideal case of coupled LSPs between two closely spaced MNPs, closely representing the experimental system, though the description of coupling is valid for many other cases involving SPs. Furthermore, in each example of coupled systems, the physics can be reduced to interactions between neighbouring charge distributions. Understanding the simple dimer system is therefore important to fully understand more complex geometries.

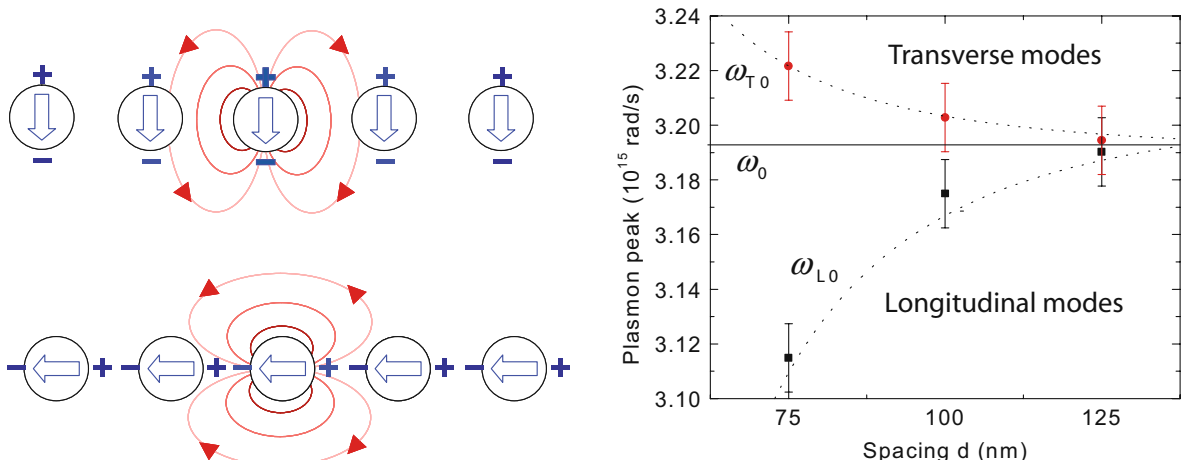


**Figure 1.6: Experimental and theoretical plasmon coupling.** Dipolar plasmons in chains of spherical AuNPs couple depending on field orientation [10] (left). Experimentally measured plasmon resonance energies in coupled AuNP chains show the gap-dependent tuning due to coupling [32] (right). The dotted line corresponds to a  $r^{-3}$  point dipole model.

In the simplest description, the Coulomb interaction between free electrons in adjacent MNPs introduces an additional coupling force, pulling charge towards the gap between metallic surfaces. A greater amount of charge accumulates on the gap-facing metallic surfaces. As particles move closer together this force grows, more strongly confining the charge and increasingly polarising the gap region. The resonance frequency of the individual plasmon mode shifts from  $\omega_0$  by  $\Delta\omega$  depending on the strength of coupling. The sign of  $\Delta\omega$  depends on whether the coupling is attractive or repulsive. Similar to coupled oscillators, the two coupling configurations (normal modes) are the in-phase bonding and anti-phase anti-bonding modes. Compelling evidence for these modes has been seen many times, with particularly good results found using chains of AuNPs [32], as shown in Figure 1.6. In general, light drives the free electrons of two sub-wavelength particles in phase resulting in the bonding configuration and a redshifting coupled plasmon with decreasing interparticle separation.

The primary effect of this kind of plasmon coupling is increased confinement of the electric field to the dielectric gap medium, leading to much larger field enhancements that can be exploited for sensing. For a strongly confined gap mode there is very little field in the metal with almost all field confined within a small lateral mode within the gap [42]. This is known as a plasmonic “hot spot”. Through this mechanism alone the field enhancement  $|E/E_0|$  can be increased by more than an order of magnitude [43, 44]. Hence, in recent years, the interests of the plasmonics community have shifted from individual plasmonic nanostructures to coupled systems in order to maximise nano-optical performance. This has led to the progression into sub-nm plasmonic cavities, the study of which is a focus of this project. The development of a theoretical model for such small systems begins with the classical models of plasmon coupling with additional complexity added until quantum mechanical effects become apparent.

### 1.2.1 Classical Models of Plasmonic Coupling

Two analytical classical models exist to describe plasmon coupling. The first and simplest model continues the description of the dipole plasmon present in small (quasistatic) MNPs and introduces dipole-dipole interactions. The second model of plasmon hybridisation is more complex and successfully models higher order modes of charge oscillation.

#### Dipole-Dipole Model

In its simplest case, interactions between dipolar plasmons in small MNPs appear similar to dipole-dipole interactions [32, 33, 45–47]. These exhibit the same behavioural dependence on separation and relative orientation with respect to the incident field. Examples of some commonly considered dipole-dipole interaction geometries are shown in Figure 1.7. In each situation the electric field incident on a dipole  $\mathbf{p}_1$  is perturbed by the presence of a second dipole  $\mathbf{p}_2$  a distance  $r$  away, whose fields as given in Eq. 1.28 are superimposed onto the

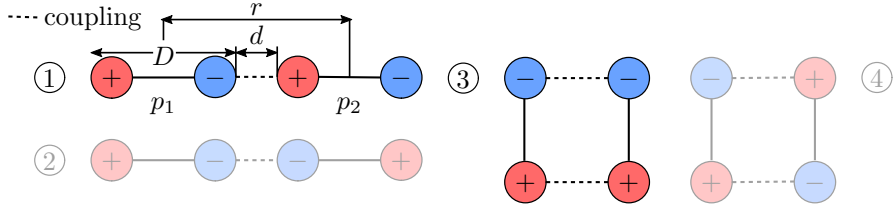


**Figure 1.7: Diagram of dipole interactions.** The distance between dipoles of length  $D$  is  $r$  with an edge-to-edge separation  $d$ . Configurations 1 and 3 are comparable with plasmon coupling as a result of sub-wavelength structures being driven by a single external light field. Configurations 2 and 4 are generally unphysical or non-radiative in plasmon dimers without asymmetry or phase retardation.

incident field at the location of  $\mathbf{p}_1$ . The result is in an effective field given by,

$$\mathbf{E}_{\parallel}(\mathbf{p}_1) = \mathbf{E}_{0,\parallel} + \frac{\mathbf{P}_2}{2\pi\epsilon_0\epsilon_d r^3}, \quad (1.37a)$$

$$\mathbf{E}_{\perp}(\mathbf{p}_1) = \mathbf{E}_{0,\perp} - \frac{\mathbf{P}_2}{4\pi\epsilon_0\epsilon_d r^3}, \quad (1.37b)$$

where  $\parallel$  and  $\perp$  denote the orientation of dipoles relative to the dimer axis. The sign of the second term in each equation determines the effect of coupling whilst its strength falls as  $r^{-3}$  due to  $V \propto p_1 p_2 r^{-3}$  [48]. The polarisability of the MNP is then modified by the interaction field, changing the frequency at which it becomes resonant. For two dipoles aligned end-to-end ( $p \parallel r$ ) and driven in phase, coupling is attractive (increased  $E$ , Eq. 1.37a), leading to a decrease (redshift) of the resonant frequency. Conversely, the interaction between two dipoles aligned side-by-side ( $p \perp r$ ) is repulsive (decreased  $E$ , Eq. 1.37b), causing an increase (blueshift) of the resonant frequency. These describe the in-phase interactions between two dipole. Anti-phase configurations, as shown in Figure 1.7, behave in the opposite manner to the in-phase counterparts as the direction of the Coulomb force reverses. These configurations are often ignored in quasistatic dimers since light can only drive in-phase oscillations. Electron-based techniques such as EELS are instead used to probe these 'dark' modes. Using EELS with AuNP chains, the validity of the dipole approximation was confirmed, showing good agreement with the experimental data shown in Figure 1.6 [32].

The dipole-dipole model is only an approximation to actual plasmonic coupling and does not adequately account for the spatial charge distribution. It can be somewhat improved by taking into account the finite particle size. Since the internal restoring force within particles, scaling as  $D^3$ , contributes to the potential, the interaction energy goes as  $(r/D)^{-3}$  as opposed to  $r^{-3}$  [49]. Furthermore, this quantity is redefined to better represent a dimer using the gap size,  $d$ , as  $(d/D) = (r/D) - 1$ . The resonant wavelength shift due to attractive coupling can

then be approximated using a “plasmon ruler” equation [49, 50],<sup>14</sup>

$$\frac{\Delta\lambda}{\lambda_0} = a \exp \left[ -\frac{(d/D)}{\tau} \right], \quad (1.38)$$

where  $a$  is the coupling strength and  $\tau$  is a decay constant. In essence, this model describes an interesting phenomenon - that plasmon coupling is scale invariant. Dimers comprised of larger particles interact more strongly for the same separation than smaller dimers. However, their relative shifts depend on how the gap size compares with the particle size. In recent years this relation still shows good agreement with experimental data but the approach remains limited to describing only dipolar modes in simple geometries [34].

### Plasmon Hybridisation

A slightly more complex model, known as plasmon hybridisation, was developed to more generally explain the formation and behaviour of coupled modes [12, 52, 53]. In this model, plasmon resonances are mechanically modelled as resonant oscillations of an incompressible fluid confined within an equilibrium geometry [12]. The plasmon resonances of a more complex particle geometry are then solved by decomposing it into coupled resonances of two simpler

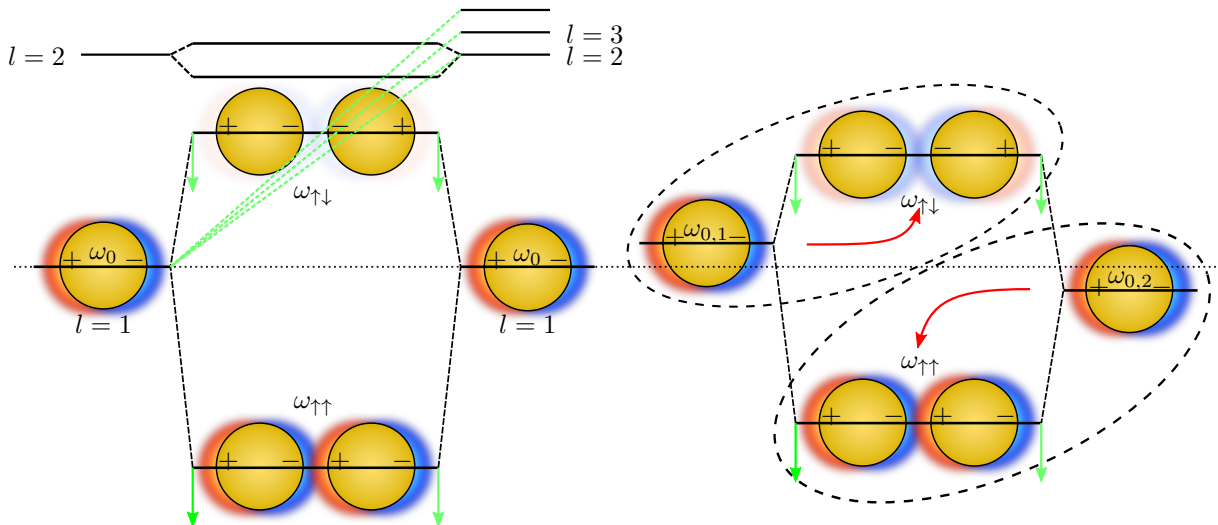


**Figure 1.8: Diagram of plasmon hybridisation between coupled plasmons in a nanoparticle dimer.** Plasmons are coupled along the dimer axis. Coupling leads to bonding and anti-bonding modes for each set of interacting  $l$  modes (left). Interaction with higher order  $l$  modes lowers the overall energy of lower order coupled modes (green lines). Only the bonding ( $\omega_{\uparrow\uparrow}$ ) mode in the symmetric (homo-)dimer has a net dipole moment and is therefore observable. Cancellation of the net dipole moment means the anti-bonding ( $\omega_{\downarrow\downarrow}$ ) mode remains optically dark. On the contrary, asymmetry in a (hetero-)dimer means both modes stay bright (right). In this case, the lower and higher energy individual modes shift to form the bonding and anti-bonding hybridised modes, respectively. This diagram is adapted from [52].

<sup>14</sup>The exponential approximates a more complex power law [51].

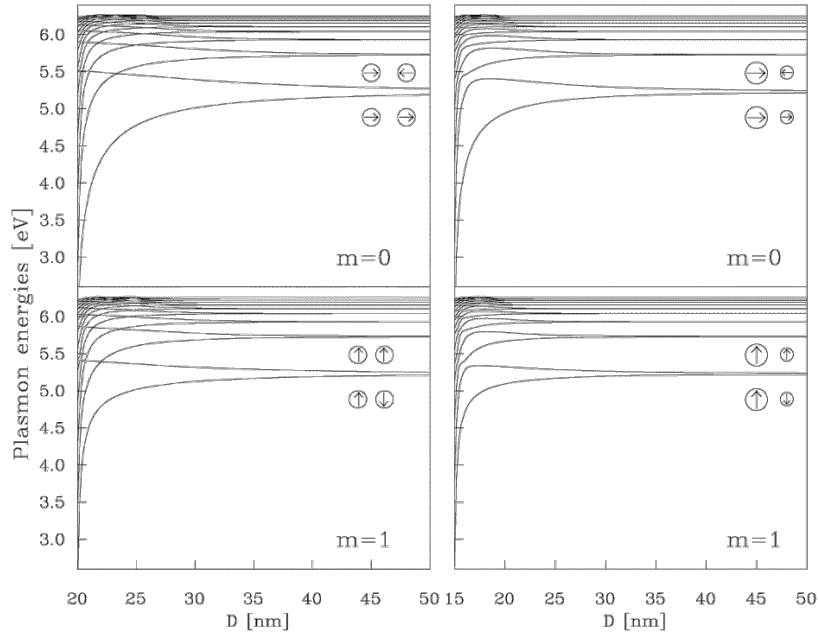


**Figure 1.9: Hybridised plasmon energy shifts for spherical AuNP dimers.** Homodimer (left) and heterodimer (right) plasmon energies are calculated in both the axial (top) and transverse (bottom) coupling configurations. Spheres are 10 nm in diameter in the homodimer and 10 nm and 5 nm in the heterodimer.

particle geometries [12, 53]. This is done in analogy with the ideas underpinning molecular orbital hybridisation and the hybridisation of quantum energy states. Using this logic, the theory equally describes the plasmon resonances of two coupled simple particle geometries [52] or a particle coupled with its image charge in a surface [54]. Under these circumstances, the multipolar modes of each of the individual dimer particles energetically split into two hybridised modes representing the bonding (in-phase) and anti-bonding (anti-phase) configurations. This behaviour is shown in Figure 1.8.

Unlike the dipole-dipole model, plasmon hybridisation is capable of predicting higher order multipolar modes in a coupled dimer system as well as dealing with more complex geometries. It is therefore valid for describing larger dimer geometries and smaller gap sizes. As with dipole-dipole interactions, the bonding and anti-bonding hybridised modes redshift and blueshift from their initial mode positions upon decreasing the separation, respectively. These shifts in the plasmon energies are shown in Figure 1.9. However, the addition of higher order modes to the classical description of plasmon coupling, and their interaction with adjacent modes of similar energies, modifies the rates of each mode's shift, as shown by the green lines in Figure 1.8 [52]. These interactions leads to a further redshift of each affected mode, though only in the case of small gaps or larger particles when higher order modes are excited.

In each classical approach it is the resulting dipole moment of each coupled mode that dictates its radiative properties. The in-phase bonding mode exhibits a large dipole moment and strongly couples with light whereas the anti-phase anti-bonding mode has no net dipole

moment in a symmetric, quasistatic system and thus remains dark. This remains the case until the anti-bonding dimer mode acquires a finite net dipole moment, either through particle asymmetry (difference material, size or shape) or phase retardation across the dimer (large particles, non-quasistatic),<sup>15</sup> at which point it becomes more radiative and hence experimentally observable using optical methods. Alternatively, local excitation of specific charge distributions using EELS allows for measurement of dark modes [55, 56]. Should both bonding and anti-bonding modes be bright and gaps decrease enough that a blueshifting anti-bonding mode approaches on a higher order redshifting bonding mode, an anti-crossing will occur and modes exchange symmetry. This causes anti-bonding modes to eventually redshift into geometrical contact.

Whilst each of the previously described analytical models has found some success in describing experimentally observed plasmon coupling in simple systems, their approaches are limited in scope. Neither model directly calculates electrodynamics and solves the actual electromagnetic problem. Instead, they use analogies to similar electromechanical systems to provide a useful insight into the mechanism of plasmon coupling. The electrodynamics of a particular plasmonic problem are now often solved using computationally demanding, numerical techniques, in which the electrodynamics are solved at each boundary within a system.

### 1.2.2 The Dynamical Optical Response of Plasmonic Dimers: Transitioning from Capacitive to Conductive Plasmonic Coupling

Using modern numerical simulation techniques, such as the boundary element method (BEM) and finite-difference time-domain (FDTD) approaches, the full separation-dependent optical response of a plasmonic dimer has been calculated as particles transition from non-interacting to coupled through into geometrical contact [42]. In these calculations, the lowest order plasmons hybridise, redshift and more intensely scatter as the separation decreases, with higher order modes eventually emerging. Classically, this leads to a large number of modes being present in nanometric-size gaps. The lateral confinement of the field between particles of radius  $R$  separated by a gap of width  $d$  is estimated as  $w = \sqrt{Rd}$  [42]. As higher order modes become more intense, scattering from lower order modes decreases. Despite this, their field enhancement continues to rise [57]. These plasmons become so confined that they no longer couple with the far-field. This behaviour continues until particles are nearly touching into geometrical contact.

Once touching, bonding hybridised plasmons abruptly transition into charge transfer plasmons (CTPs) - charge oscillations spread across the full extent of the connected dimer. These

---

<sup>15</sup>Phase retardation of the driving field across the dimer breaks the coupling symmetry, allowing anti-phase modes to be excited.

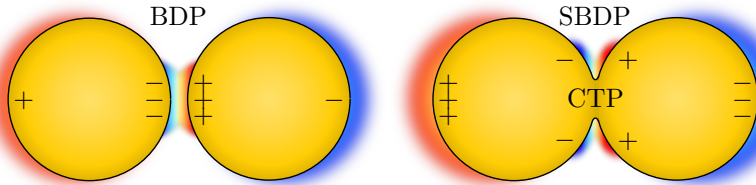


**Figure 1.10: Diagram showing the emergence of charge transfer and screened bonding (crevice) plasmons on geometrical contact in a nanoparticle dimer.** The field generated by the bonding dimer plasmon (BDP) is screened from the gap by the conductive contact, forcing capacitive coupling to the crevice gap in the form of the screened bonding dimer plasmon (SBDP). The dominant charge oscillation is then the charge transfer plasmon (CTP) through the conductive bridge and across the whole structure.

are widely observed in geometrically contacted or overlapping plasmonic systems [33, 58]. A dipolar CTP emerges at lower energies (considered to be the equivalent of a monopolar dimer mode) as screened hybridised plasmons are expelled out of the gap, transitioning into higher order CTPs due to their similar charge distributions [42, 59–61]. Their resonances blueshift, diminishing in intensity and broadening in width as a result of significantly increased currents. The lower energies of CTPs are associated with a spatially larger dipole, as shown in Figure 1.10, suggesting they should blueshift with increasing particle overlap. Their broad width compared with capacitively coupled plasmons is caused by dissipation in the junction and can be linked with behaviour described by Eq. 1.12.<sup>16</sup>

Classical predictions of plasmon coupling break down at small, sub-nm gaps where the continuum of excited higher order modes redshift to a singularity as  $d \rightarrow 0$ , and the field enhancement increases infinitely. This behaviour is completely unphysical and is rectified once non-locality and quantum mechanical effects are considered. A comparison of the models taking these into account is shown in Figure 1.11. Quantum mechanical effects begin to affect plasmon coupling under two conditions - either the particles become sufficiently small that quantum non-locality and non-local effects (finite, non-negligible electron wavefunction spill-out from the particle) become important or the gap size decreases to scales on which quantum tunnelling and non-locality of the gap surfaces can no longer be ignored.

Non-locality, the spill-out of electrons from the surface of the metal, smooths the gap geometry, and consequently the spectral trends. The redshift into contact is heavily reduced compared with classical predictions. Smoothing of the sharp edges in the gap rectifies the continuum of higher order modes, which are then harder to excite, leaving only the most fundamental dimer modes. Redshifts are reduced since electrons move further into the metal on approach, suppressing coupling [62]. The emergence of CTPs and screening of the bonding

<sup>16</sup>For a spherical MNP dimer with a bonding hybridised dipolar plasmon (BDP) and bonding hybridised quadrupolar plasmon (BQP) the corresponding CTP modes are typically labelled as the CTP and CTP'. The CTP' is often labelled as the screened bonding dipolar plasmon (SBDP) due to the similarities in the charge distributions between a second order CTP and first order bonding mode.

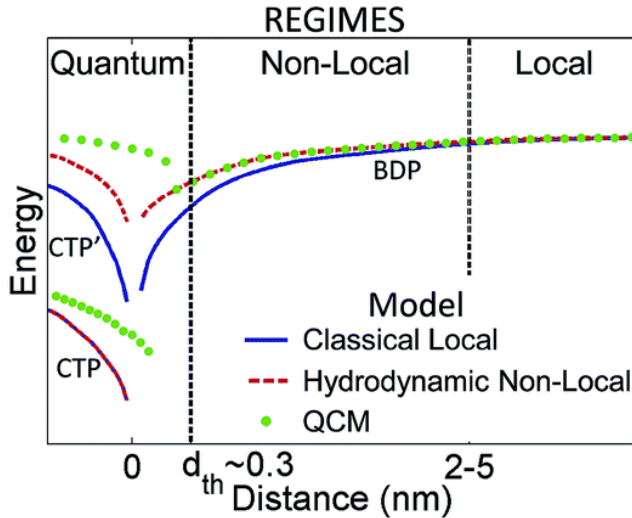


**Figure 1.11:** Calculated plasmon energies of a spherical AuNP dimer as a function of gap separation using a number of computational models [62]. The classical local approach is valid for separations greater than 2 nm. Below this non-locality smooths the gap and adequately describes mode behaviour until 3 Å. At this point quantum models must be used. Figure taken from [62].

hybridised modes prior to geometrical contact are predicted only once quantum charge transfer effects are accounted for. The onset of quantum tunnelling means charge is transported across the gap without requiring geometrical contact, neutralising some of the accumulated plasmon charge. Tunnelling is then followed by ballistic charge transport prior to returning to a classical description of plasmonics. These two effects, due to their significance in dimer systems, are considered in more detail.

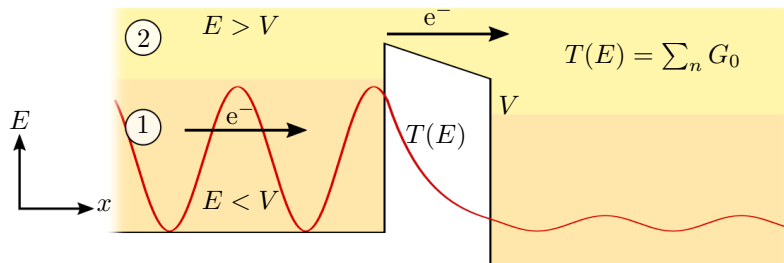


**Figure 1.12:** Diagram of quantum charge transport between two reservoirs of free electrons. If the Fermi energy of electrons is below the barrier potential (1) then there is a finite transmission probability  $T(E_F)$  of tunnelling through the barrier. If the Fermi energy becomes larger than the potential barrier electrons are free to move through a number of quantised conductance channels of conductance  $2e^2/h$ .

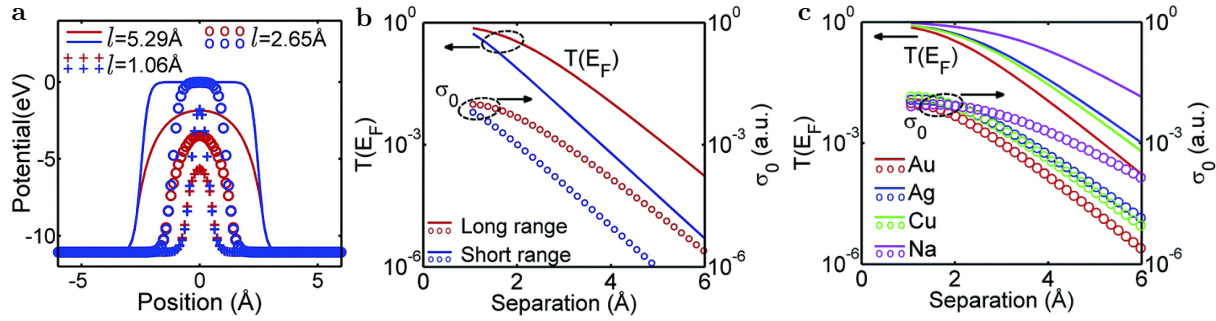


**Figure 1.13: Potential barrier shapes for various gap widths and tunnelling transmission probabilities as a function of separation and material [62].** Calculated potential barrier shapes between two Au particles as a function of separation (a) with corresponding transmissions (b). The inclusion of long-range image charge interactions is compared with a simple short-range barrier model. Realistic barrier shapes are more rounded than the simpler rectangular assumption. Overlap between rounded potential edges decreases the barrier height with reduced separation. Tunnelling increases exponentially as the gap width reduces, with increased tunnelling caused by the smaller rounded barriers. Transmission depends on the work function of a material with differing transmission probabilities at a given separation (c).

### Quantum Charge Transport: Electron Tunnelling and Ballistic Transport

The quantum charge transport properties of a system consisting of two reservoirs of free electrons separated by a potential barrier are determined by how the height of the potential barrier compares with the Fermi energy of each reservoir. For two metals separated by an insulating gap the potential barrier will be larger than the Fermi level. Classically, electrons with energies below the potential barrier cannot reach the other side. Electrons can only conduct through via quantum tunnelling, in which electrons incident on thin barriers have a finite probability of passing directly through the barrier as opposed to going over it. This is shown in Figure 1.12.

The potential barriers and transmission probabilities of a tunnel junction between two reservoirs of Au are shown in Figure 1.13. In a simplistic model, the potential layout is considered as a 1D rectangular barrier and the tunnelling probability increases exponentially with decreasing barrier width,  $d$ , going as  $T = e^{-\beta d}$ , where  $\beta$  is a decay parameter [63].<sup>17</sup> Many different mathematical descriptions of this phenomena exist [64, 65], especially after the invention of STM, that predict the conductance and resulting current density as electrons tunnel through an arbitrary potential landscape. This is in part due to the large number of parameters that influence tunnelling (e.g. work function, barrier potential, barrier shape, applied bias, temperature, charge hopping [65]) and the extension of it into 3D gap morphologies, however the exponential decay is always present.<sup>18</sup> The current density is therefore expected to follow

<sup>17</sup>For a simple rectangular barrier of height  $V_0$  the transmission  $T = |t|^2$  is given by,  $T = e^{-2\sqrt{\frac{2m}{\hbar^2}(V_0-E)}d}$ .

<sup>18</sup>At least within a low bias approximation, which is generally valid in the context of this thesis.

[66],

$$J = J_0 e^{-\beta d}, \quad (1.39)$$

where  $J_0$  is a saturation current density. This behaviour holds for large gap sizes but begins to fail in small ( $2 \text{ \AA}$ ) gaps where the rectangular barrier shape assumption no longer holds (Figure 1.13a,b). The barrier height begins to decrease with separation on overlap of the rounded edges. Tunnelling then becomes even more likely as the separation decreases. Since the transmission depends on the Fermi energy of free electrons in a material and the potential of the barrier region in between, different materials have different tunnelling responses. For example, tunnelling is far stronger in Na than in Au (Figure 1.13c) [62]. Finally, the current generated by tunnelling depends on the number of tunnelling channels available in a junction and the transmission coefficient of each channel [67].

Once the barrier falls below the Fermi level (at  $\sim 1\text{--}2 \text{ \AA}$ ), provided that the contact is short enough that motion is ballistic (no scattering), conduction electrons can move freely between the two reservoirs via a number of discretely quantised, 1D conduction channels under the application of an applied bias. This bias in the plasmonics case stems from the field induced by light. Each channel has a transmission probability  $T(E_F) = 1$  and a conductance given by  $G_0 = 2e^2/h$ , the conductance quantum [68]. The total conductance depends only on the number of open channels, a quantity depending typically on the width of the conductive region. This results in a conductance described by the Landauer formula<sup>19</sup> [68],

$$G = \frac{2e^2}{h} \sum_n T_n(E_F) = n G_0, \quad (1.40)$$

where  $n$  is the number of transmission channels. Though still firmly in a quantum domain, ballistic transport is a form of conductive contact as opposed to a tunnelling phenomenon. Classical behaviour is only recovered if the length of the constriction increases to the point at which electrons begin to scatter or the width increases to allow many channels. In this event, the conductance is classified as diffusive with a conductance given by  $G = \sigma A/d$ .

## Quantum Charge Transport in Plasmonic Nanogaps

The effects of quantum charge transport were first predicted in small ( $R < 2 \text{ nm}$ ) NaNPs using full quantum mechanical, time-dependent (TD) density functional theory (DFT) calculations [67]. Since these calculations consider the behaviour of each electron, they are currently limited in complexity to small systems containing less than 2000 electrons. Quantum effects in larger metallic nanostructures are predicted by the quantum corrected model (QCM), a classical model which includes the effects of non-locality and uses an effective gap dielectric function

---

<sup>19</sup>Full derivation of the Landauer equation and quantised conductance is found in the appendices.

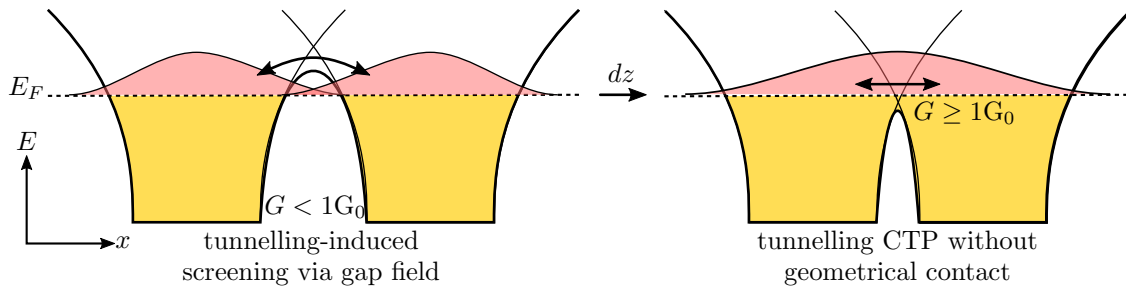


**Figure 1.14: Diagram of the charge transfer process in a nanoparticle dimer.** Electrons are considered non-local and spill out from the gap surfaces. Long-range image charge interactions also further round the potential barrier. Tunnelling at large distances neutralises optically-driven charge accumulation on gap surfaces, reducing coupling. At smaller separations the particle Fermi level can become greater than the gap potential barrier, permitting conduction instead of tunnelling. This is the origin of gap current and CTP excitation.

that takes into account the conductivity induced by quantum effects using pre-calculated values from TDDFT [57]. Both the QCM and TDDFT show agreement on the effects of tunnelling and conduction on plasmon coupling in NaNPs, with QCM predictions of the plasmon energies in a AuNP dimer shown in Figure 1.11. Experimentally, evidence of quantum transport effects in plasmonic gaps has recently been found using optical spectroscopy [69–71], EELS [72], SERS [71], photoluminescence [73] and third-harmonic generation measurements [74].

In numerical simulations, the onset of tunnelling creates a conductive bridge through which electrons can transmit during each half optical cycle. Charge transfer across the junction neutralises some of the plasmon charge on gap surfaces, locally preventing charge accumulation and lessening the local capacitive interaction. This is the screening effect. Electron tunnelling increasingly screens coupling leading to a reduction in the rate of redshift. The appearance of this additional contribution to coupling signifies entry into the *crossover* regime [67]. At these separations, typically 5 Å in Na, the barrier remains above the Fermi level. The most prominent effect of screening is a drastic decrease of the field enhancement in the gap as bonding hybridised modes are gradually expelled from the gap [57, 67]. In theory, this prevents small gaps from being useful as SERS structures but instead provides a method of optically studying electron transport on sub-nm length scales, motivating the need to fully understand such effects.

The conductance provided by gap sizes characteristic of tunnelling is too small to excite CTPs, hence only screening is initially observed. Once the gap size reduces to the point at which the barrier falls below the Fermi level a dimer transitions into a conductive state where  $T(E_F) = 1$  and conductances are given by Eq. 1.40. This is the *conductive* or *CTP* regime. A diagram showing the changeover in conduction mechanisms is shown in Figure 1.14, similar to the DFT calculations presented in [67]. In recent quantum simulations this critical gap width is found between 1–2 Å. A similar drop in barrier heights below the work function of Au is found in Figure 1.13a between 2.65 Å and 1.06 Å. The free flow of electrons permits a

large amount of current through the junction and enables CTP excitation [67]. The current immediately increases screening so much that bonding hybridised plasmons decouple and undergo a blueshifting transformation into CTPs. In initial quantum calculations [67] the fundamental CTP is not shown but is found in later TDDFT calculations appearing near to geometrical contact once the conductance rises sufficiently [57, 72].

Though initial simulations considered only small NaNPs it is proposed that in larger nanoparticle dimers the boundary to the quantum regime would be extended to larger separations as larger nanoparticles have more closely spaced energy levels (reduced quantum size effects) and therefore more available conductance channels [67]. In essence, this means that the conductance required to cause these effects remains the same but is achieved through the cumulative contribution of many individual conduction channels. The QCM seemingly reproduces this effect with CTP excitation and blueshifts occurring in  $R = 25$  nm Au particles at around the same 2–3 Å separation as in  $R = 2.17$  nm Na particles, despite the lower rate of tunnelling between Au surfaces. This indicates that a larger surface generates the same tunnelling conductance as a smaller, more conducting junction, which is enough to produce the same amount of charge transfer in one optical cycle.

A simple estimation of this critical distance is given in [69]. The conductive regime is said to dominate once the charge stored in a plasmon becomes less than the charge involved in charge transfer, i.e. the fraction of conductive charge is greater than 50%. The tunnelling conductivity in a rectangular barrier model is,

$$\sigma(d) = \frac{3k_e e^2}{4\pi h} e^{-2k_e d}, \quad (1.41)$$

where  $k_e = \sqrt{2m\varphi}/\hbar$  is the electron wavenumber at the work function,  $\varphi$ . The distance at which this leads to a majority of charge transfer is calculated as,

$$d_{QR} = \frac{1}{2k_e} \ln \left[ \frac{3k_e \lambda \alpha}{2\pi} \right], \quad (1.42)$$

where  $\lambda$  is the wavelength of the plasmon and  $\alpha = 1/137$ , the fine structure constant. Evaluating this for Au ( $\varphi = 4.8$  eV) at an 850 nm plasmon wavelength yields a critical separation of 1.6 Å. If instead the larger conductivity from DFT is used, the equation predicts a critical gap size of 3.1 Å, the same value as is shown in QCM spectra. This is the point at which plasmons change from being majority capacitively coupled to majority conductively coupled.

Preliminary experimental measurements of the optical scattering from a dynamic spherically-tipped Au AFM probe dimer clearly show the aforementioned effects. Two coupled plasmon resonances, denoted A and B, begin to weaken during the final 7 Å of the approach into contact (Figure 1.15a) [69]. Distances are determined by comparing with QCM spectra. Modes A and B blueshift upon decreasing past a critical separation of 3 Å and begin to regain intensity.

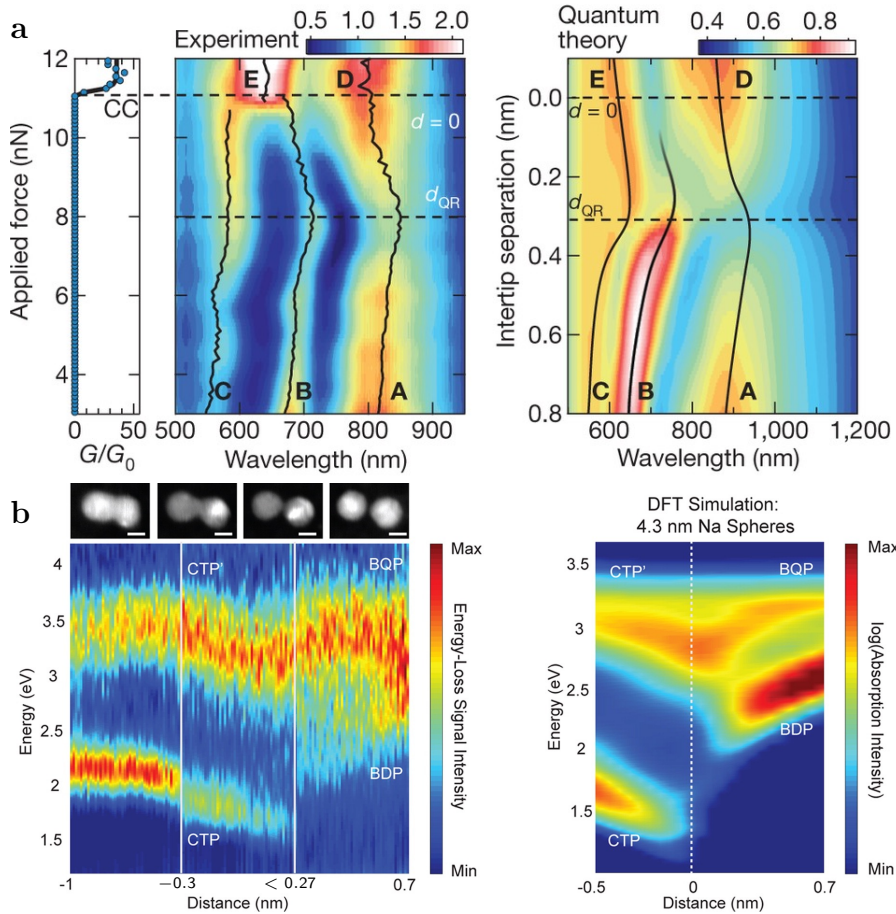


**Figure 1.15: Examples of experimental measurements of the effect of quantum tunnelling on plasmonic gap systems through direct monitoring of the plasmon resonances.** (a) Supercontinuum dark-field scattering measurements of two 300 nm diameter spherical Au tips in a dimer configuration with reducing separation, transitioning below 1 nm and into the quantum regime [69]. (b) EELS measurements of 10 nm AgNPs being induced closer together by the electron beam [72].

A mode, C, strengthens going into contact. These are the signatures of bonding hybridised modes transforming into CTP modes as field is expelled from the gap and conductive channels bridge the gap. Agreement between experimental and theoretical spectra also reaffirms the assumption that the smooth changeover between capacitive and conductive plasmons occurs once charge is split equally between them.

Though experimental tip dimer spectra and QCM spectra have some discrepancies due to the difficulty in simulating such large tip structures, they qualitatively agree. Further agreement with DFT calculations is found in EELS measurements on 10 nm AgNP dimers, brought together under the influence of the electron beam (Figure 1.15b) [72]. In this system the dimer exhibits screening at 5 Å and the blueshifting transformation between bonding modes and CTPs begins at 3 Å along with the excitation of the fundamental CTP. The agreement between both experiments, the QCM and DFT calculations reinforces the idea that quantum

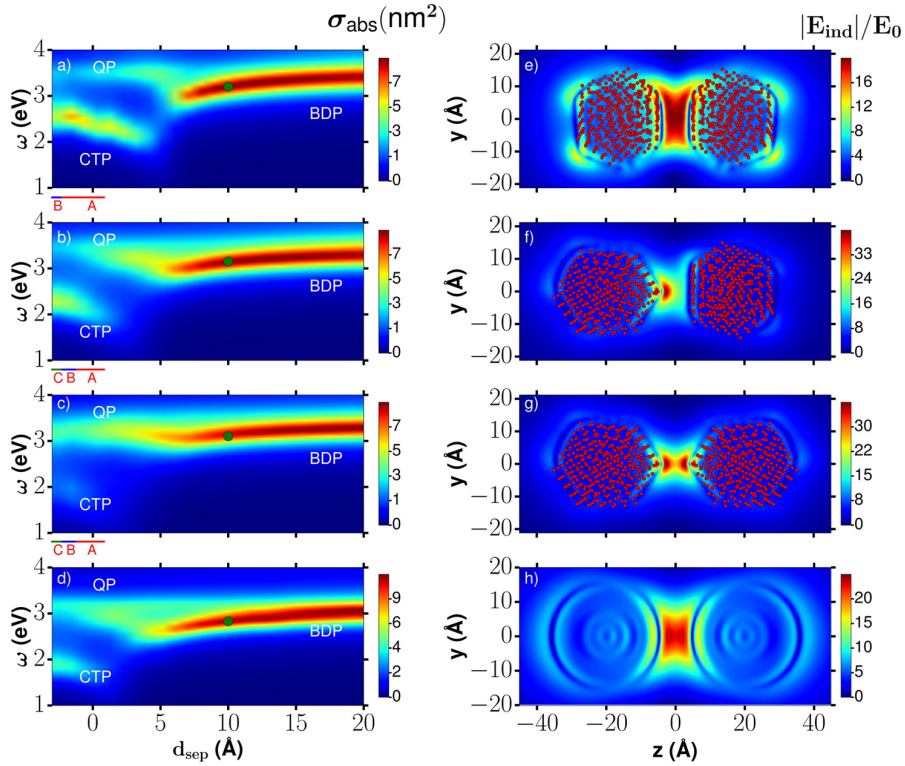


**Figure 1.16: TDDFT calculations of 16 Å faceted NaNP dimers arranged with different facet alignments [75].** Aligned facets leads to the smallest field enhancement and the earliest onset of charge transfer effects at 5 Å. Vertex alignment results in an atomic-scale lightning rod effect and increased field localisation. CTP excitation is more difficult in this configuration, occurring at 0 Å, due to the small contact but screening is made easier for the same reason, occurring at 7 Å. The figure is taken from [75].

tunnelling screens plasmon coupling and the rising conductance after ballistic conductive contact leads to the rise of CTPs. The observation of a critical distance of 3 Å in many systems of different sizes, shapes and metals is also intriguing and poses further questions of what exactly the conductance is at that point.

A small number of recent experiments have also now began to report effects attributed to conduction and quantum tunnelling. Alkanedithiol molecules of various lengths have been used to discretely tune the gap separation of AuNP dimers, with attenuation and blueshifting of the BDP with molecules smaller than pentanedithiol [70]. Similar results are found when using intercalating surface-assembled monolayers (SAMs) [66]. Further investigations into sub-nm plasmonic gaps have also shown behaviours attributed to quantum tunnelling, though inferred from properties depending on the field enhancement as opposed to direct measurement of SPRs. A decrease in signal intensity in both the SERS peaks [71] and photoluminescence [73] in nano-gap systems, for example, are signatures of quantum tunnelling screening the coupled plasmon field.

A final feature to note about quantum effects is their variability with gap morphology. It

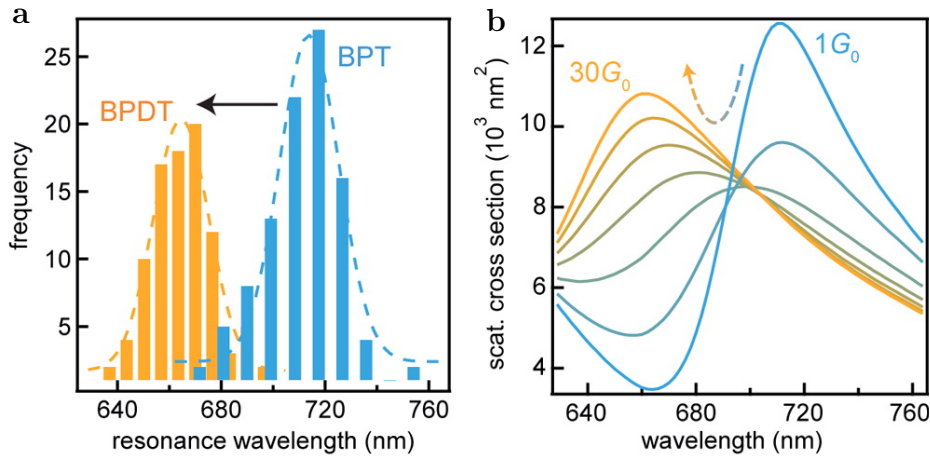


**Figure 1.17: Experimental and theoretical scattering spectra of 80 nm AuNP on a planar Au mirror separated via variable conductance molecular spacer layer [76].** Variable conductance molecular SAMs are formed from fractional mixing of BPT (insulating) and BPDT (conductance). The blueshift and attenuation of the coupled plasmon begins at  $2G_0$  with the screened mode emerging once  $G > 5G_0$ .

has recently been shown theoretically that atomic-scale morphology changes can dramatically alter the plasmonic response through the sub-nm regime [75]. This is demonstrated by considering 16 Å faceted NaNPs dimers in various configurations, shown in Figure 1.16. With flat surfaces aligned the conductance is maximised with a CTP and a fast blueshift seen as early as 5 Å. In contrast, with facet vertices aligned, a CTP only begins to emerge after contact between atoms. Screening in this arrangement is observed earlier at around 7 Å, likely due to charge only having to neutralise a small surface area. The facets demonstrate an atomic lightning rod effect that increases the field in the gap whilst minimising the conductance. All other configurations average to the expected result predicted using a spherical particle model. This demonstrates that experiments can in some sense become limited by surface roughness or even atomistic surface defects.

### Limits of Critical Behaviour in Conductive Plasmonic Nanogaps

Both the blueshifting portion of the screening effect and CTP excitation require a conductance threshold to be surpassed in order for these effects to occur. Thresholds have been defined for a dimer containing a classical conductive linker, where the gap between particles of radius  $R$  has a width  $d$ , conductivity  $\sigma$  and linker radius  $a$  [59]. The formation of screened plasmons occurs at low conductances with a critical conductance for the dipolar bonding plasmon given by,

$$G_{\text{SBP}} = 2\epsilon_0\omega_{\text{BDP}} \frac{a^2}{d}. \quad (1.43)$$

Reducing the conductance to a conductivity by removing a factor of  $\pi a^2/d$  shows that screening is intrinsically independent of geometry and depends only on a critical conductivity given by,

$$\sigma_{\text{SBDP}} = \frac{2\varepsilon_0\omega_{\text{BDP}}}{\pi}. \quad (1.44)$$

For larger contact widths or shorter linker lengths the conductance threshold increases to overcome the increased capacitive coupling. Experiments maintaining a fixed geometry whilst increasing the gap conductivity using fractional mixing of similar conductive and insulating SAMs have succeeded in showing a blueshift of coupled plasmons with an estimated  $2G_0$  threshold [76], as shown in Figure 1.17. A similar  $2G_0$  threshold is also found in theoretically considered 1 nm dimer linkers [59].

A second, much larger, threshold exists for CTP formation, occurring at,

$$G_{\text{CTP}} = \varepsilon_0\omega_{\text{CTP}} \frac{R^2}{d}, \quad (1.45)$$

which can similarly be reduced to a critical conductivity,

$$\sigma_{\text{CTP}} = \frac{\varepsilon_0\omega_{\text{CTP}}}{\pi} \left( \frac{R}{a} \right)^2. \quad (1.46)$$

Unlike screening, CTP formation depends not only on the conductivity but also the junction geometry. The geometry factor ( $R/a$ ) represents the ratio between the total charge in the particle and the amount which can pass through a gap with fixed conductivity. Having a large conductivity means the junction does not have to be as wide, relative to the particle size, to accommodate enough current to maintain a CTP. Hence, dimers linked by a highly conductive metallic link can sustain a CTP with only a small nanometric-scale contact area. This has been demonstrated by threading together AuNP dimers fixed with a hollow spacer molecule using high power laser pulses [61, 77].

Interestingly, qualitative agreement between QCM calculations and full quantum mechanical calculations suggest that the quantum nature of the system is of little importance. Even though the QCM uses a classical, resistive gap with conductances values characteristic of quantum transport, quantum effects on gap plasmons are accurately replicated. This implies that, despite the quantum nature of such small gaps, the effects on plasmon coupling only depend on the amount of charge transfer and not the mechanism by which it occurs. This links together work done using particle positioning [69, 72] with studies of interacting plasmonic system coupled with molecular linkers [66, 70, 76]. Quantum tunnelling and non-geometrical conductance still remains an interesting case, however, since both forms of conduction are unavoidable once gap sizes decrease below 0.5 nm. This is why the point at which the electric field is expelled from the gap is described as the quantum limit to plasmon confinement [69].

For this reason, it is important to fully understand the relations between plasmonic hot spots and sites of (quantum) charge transfer.

Although charge transfer effects have been shown in previous reports by varying the conductivity of a fixed gap, there has yet to be a report showing the optical response of a dynamic dimer structure correlated with its electronic response. It is the aim of this project to successfully demonstrate and explain the possible ways in which electrical and plasmonic phenomena are related using a dual plasmonic nano-tip dimer. Metallic nano-tips are a plasmonic geometry currently receiving significant attention from the plasmonics community. In order to use nano-tips to determine the effects of quantum tunnelling on plasmonics, their supported plasmons must first be described.

### 1.3 Plasmons in Tips

Significant efforts have been made to advance nanoscale surface characterisation by developing new optical tools and integrating optics into existing nanoscale topological measurements. Metallic tips were investigated due to the widespread use of scanning probe microscopies (SPMs), such as atomic force microscopy (AFM), and scanning tunnelling microscopy (STM). The similarity in size between metallic nanostructures and the sub-wavelength-size apex of tips initially suggested that visible plasmons would be expected, enabling resonant near-field enhancement. Prior to any spectral characterisation studies to understand their near-field response, tips were applied in combined SPM-optical microscopes to achieve sub-wavelength localisation and enhancement of optical signals. As the next logical step from surface-enhanced Raman scattering (SERS) and scanning near-field optical microscopy (SNOM), the sharp apex of tips were exploited to develop the spin-off techniques of tip-enhanced Raman scattering (TERS) [78–81] and apertureless scanning near-field optical microscopy (a-SNOM)<sup>20</sup> [82–87]. These are also known collectively as tip-enhanced near-field optical microscopy (TENOM).<sup>21</sup>

The concept for TENOM was first proposed in 1985 [88] but it was not until 2000 that reports first emerged using tips to enhance Raman spectroscopy [78–81]. All measurements were carried out in inverted microscopes with either an AFM [78–80] or STM [81] mounted on top. Two of the initial measurements suggest the overall Raman enhancement has a lower limit of  $\sim 10^4$  [78, 79], hence a field enhancement of around 10. A third independent measurement utilising evanescent wave excitation obtained an enhancement factor of 80 from a single tip apex, equivalent to the summed enhancement of many SERS hotspots on a Ag island film [80]. Since then Raman enhancements in the region of  $10^7$ – $10^9$  have been measured

---

<sup>20</sup>Also known as scattering scanning near-field optical microscopy (s-SNOM).

<sup>21</sup>These are also sometimes known as field-enhancing near-field optical microscopy (FENOM) since apertured techniques do not necessarily exploit plasmonic enhancement as much.

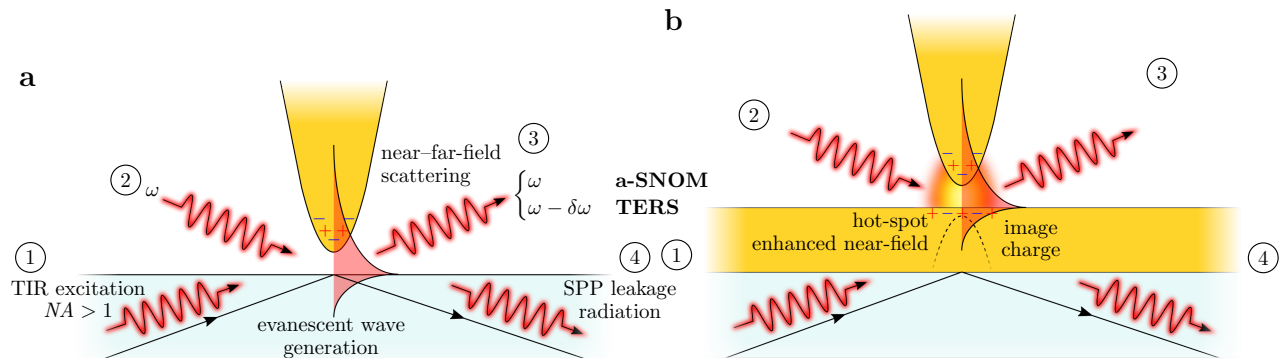


**Figure 1.18: Concepts of TENOM.** Basic TENOM systems constitute a tip and a sample (left). Tips can perturb evanescent surface waves, generated by high-NA TIR, and scatter them into the far-field (1 → 3) [90, 91]. Photons illuminating the tip can induce a weak dipole localised to the tip apex, which can scatter the near-field (2 → 3). More recent TENOM arrangements employ a metallic substrate to couple with the tip and further localise the field into a “hot spot” (right). Coupling of plasmons between the tip and the substrate can be achieved by exciting SPPs on the substrate using evanescent waves (1) or by focusing light on the MIM gap such that the tip dipole induces an image dipole in the substrate (2). Both mechanisms lead to scattering of light from the gap into the far-field (3). SPPs launched onto the planar surface (either via the tip or evanescent waves) can radiatively decay into  $NA > 1$  (1, 2 → 4) [92].

[89].<sup>22</sup> Whilst SERS enhancement factors have also increased significantly in recent years, the TENOM approach remains popular since the tip can be scanned across a sample. For this reason, techniques such as TERS are widely considered to become the successors of SERS. However, for this to be the case, nanotips require the capability to controllably and reproducibly enhance the near-field. Understanding the electromagnetic response of metallised tips has therefore become of significant importance in recent years. Since the use of tips for observing fundamental plasmonics is also a central part of this project it is beneficial to understand the underlying concepts and mechanisms of TENOM.

TENOM is ideally classified as a local excitation approach as opposed to a local scattering approach [93], though the two are not independent. Figure 1.18 shows the general approaches to TENOM. In the tip scattering approach the non-radiative near-field, comprising evanescent waves, is perturbed by the presence of the tip, leading to scattering into radiative modes. In the tip excitation approach, the tip is resonantly excited to induce a large, local, near-field enhancement and used as a sub-diffraction-limited light source, from which localised scattering can be measured. This process can be much more efficient than the pure scattering approach but depends on the optical antenna properties of the tip. In both cases, the resolution of scattering images is sub-diffraction limited and set by the size of the tip radius ( $\sim 50$  nm).

<sup>22</sup>A clear distinction is made between the field enhancement,  $|E/E_0|$ , and the Raman enhancement,  $|E/E_0|^4$ , when stating enhancement factors. In the literature the terms “field enhancement” or “enhancement factor” are generally used interchangeably between the magnitude of the near-field and the improvement in the Raman signal.

To optimally exploit light scattering from nanoscopic tips, tip-based systems have been generally designed in either the side-illumination or bottom-illumination configuration (photon paths shown in Figure 1.18), setting the collection and, more importantly, the tip excitation geometry. Side-illumination has been used successfully in a number of cases [91, 94–96] but suffers generally from far-field scattering overshadowing the near-field. More complex optical techniques, such as using polarisation-resolved or interferometric approaches, are then required to overcome this. Bottom illumination, the more dominant design, utilises evanescent waves generated by  $NA > 1$  illumination undergoing total internal reflection (TIR). TIR results in minimal background scatter outside of the illumination aperture with only the near-field scatter collected. Collection is achieved using either the central  $NA < 1$  aperture of the high  $NA$  illumination objective [97–102] or a secondary low NA objective [103–105]. Whilst this does require that both the sample and any metallic substrate are optically transmissive, evanescent wave generation can excite SPPs in both a metallic substrate and the tip once brought within the near-field. For these reasons, it is important to consider the optical geometry when interpreting any presented TENOM results.

### 1.3.1 The Electromagnetic Response of Tips

The electromagnetic response of tips can be broken down into individual components that constitute the enhancement mechanism. The two main optical components are the lightning rod effect and a resonant plasmon contribution for metallic tips [106–108]. Each component is maximised when the incident field is along the tip axis [109]. The plasmonic component has been the focus of study in recent tip-based work, however progress in sharpening tips has also led to increases in the lightning rod component. Both components are important to consider when attempting to understand optical measurements involving tips.

Regardless of plasmonic behaviour, metallic tips intrinsically exhibit a lightning rod effect under the application of an applied field, instilling a non-resonant component of near-field enhancement. From the definition of the electric field  $\mathbf{E}(\mathbf{r}) = -\nabla\varphi(\mathbf{r})$  it is clear that the electric field strongly depends on geometry, with field lines perpendicular to the equipotential conductor surface. The more curved a surface, the more compressed the field lines become around its equipotential surface due to accumulation of surface charge.<sup>23</sup> A simple model, calculated by solving Laplace’s equation for a tip-shaped electrode, shows this behaviour in Figure 1.19. Consequently, even without a plasmonic component, sharp tips provide a promising platform for localised near-field enhancement.

The expected plasmonic component also arises from the curvature of the metal-dielectric interface at the tip apex. Curvature allows for both SPP excitation and localisation at the apex due to adiabatic nanofocussing [23, 31, 110–113]. This can lead a number of localised

---

<sup>23</sup>Since  $E \propto 1/r^2$  the electric field is larger in regions of smaller curvature.

plasmon modes in the predicted spectra of tips, however none of these will have an antenna-like geometry to couple well with far-field light. As highlighted when discussing ellipsoidal MNPs, strong, antenna-like LSPs are unlikely to be excited at the apex of a sharp tip since lack of a second metal-dielectric interface prevents accumulation of the opposite surface charge to the apex. Thus, there can be no strong restoring forces or SPRs. The extended size of the typical tip structure ( $\sim 20\text{ }\mu\text{m}$ ) prevents any potential low-order antenna-like plasmons from existing. Calculations for shorter tip geometries (nanocones or nanoellipsoids) show visible-NIR LSPs [114, 115], however these redshift and diminish with increasing tip length, leaving only the smooth response of the lightning rod effect increasing towards the IR [107, 116]. The standard, sharp metallic tip geometry therefore makes for a poor *plasmonic* optical antenna unless the optically-dark SPP modes can be accessed.

Evanescence waves are capable of exciting some of these modes, with evidence for localised apex plasmons found through resonant scattering of evanescent waves [90, 91, 117], resonances in the TERS background [118, 119] and depolarised scattering images [101]. The addition of a degree of nanostructuring also allows for more localised plasmons [97, 101, 120, 121]. Spectral resonances between 600–800 nm have been observed in scattered evanescent waves from the surface of a prism by a Au tip with a W tip giving a comparatively flat spectrum [90]. These are attributed to SPPs. Shifts of  $\sim 75$ –100 nm have been observed between Ag and Au tips with a  $\text{Si}_3\text{N}_4$  underlying tip material, redshifting resonances by  $\sim 30$  nm compared with solid metallic tips [91, 117]. This dependence on both the tip metal and underlying material has been highlighted numerous times due to the prevalence of the two dominant tip geometries of sharply etched metal tips and metallised (metal-coated) non-metallic tips.

Surface roughness imparted onto metallised tips by the coating procedure is likely to introduce localised plasmonic components which light can couple to, mimicking small 10–50 nm MNPs [101]. Similar behaviour has been used to explain the origin of SERS in rough metal films [122, 123]. Each grain acts as a point at which photons couple and plasmons radiate, hence a grain located at the apex can plasmonically enhance and scatter the near-field. This

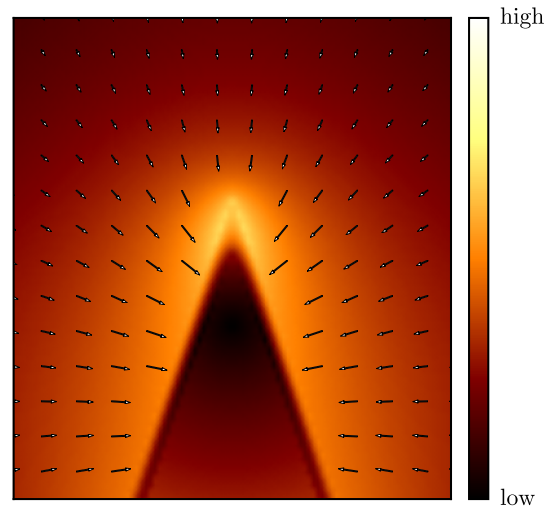


**Figure 1.19:** Calculated magnitude of the electric field around a tip showing the lightning rod effect. Compression of the field lines around the sharp corner of an equipotential surface leads to a localised, non-resonant field enhancement. Poisson's/Laplace's equation is solved for a tip structured electrode with a surface charge distribution separated by some distance from a planar metal counter electrode of the opposite surface charge.

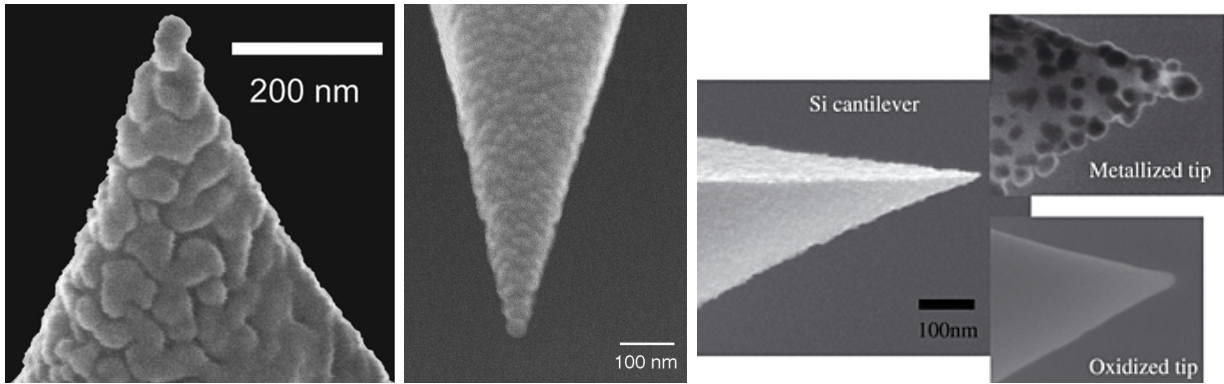


**Figure 1.20: SEM images of metallised tips exhibiting random nanostructures.** Images are taken from [101] (left), [105] (middle) and [121] (right). Each SEM shows randomised grains deposited using evaporation. These are thought to enable LSP excitation if located at the apex.

behaviour is of importance in metallised dielectric tips coated using evaporation<sup>24</sup> [97, 101, 121] or chemical reactions [120], some examples of which are shown in Figure 1.20. Even with the frequent application of TENOM, there have been very few spectral measurements of scattering from tips from which to better understand tip plasmonics. Optimum tip parameters, such as coating thickness, for maximum field enhancement are still being debated and characterisation of performance is still carried out using TERS [124].

Complete theoretical understanding of a tip's electromagnetic response is challenging due to difficulty in modelling tips. Their sub-wavelength apices and large ( $\sim 20 \mu\text{m}$ ) overall conical or pyramidal structure lead to complications when simulating their response, and approaches attempting to circumvent these limitations often cause physical inaccuracies in the result. Overly simplistic models, such as modelling only the tip apex, usually as a spherical or ellipsoidal MNP, fail to take into account the actual tip geometry, resulting in the existence of unphysical MNP-like modes at the tip apex. Similar multipolar modes are exhibited by truncated tip models with finite lengths less than  $1 \mu\text{m}$  [114, 115], behaving more like nanopyramids [125, 126]. Zhang *et al.* [107] calculate that between lengths of  $200 \text{ nm}$  and infinity a tip transitions between supporting low order LSPs, then higher order LSPs, followed by only weak SPPs. LSPs are supported only when the entire tip structure is smaller in size than the focus, allowing light to drive in-phase collective oscillations of the conduction electrons. As the tip becomes larger, phase retardation occurs and higher order LSP modes dominate. Once the tip becomes larger than the focus, the case for almost all standard SPM tips, collective oscillations are no longer possible, leaving only weak LSPs concentrated at the apex and SPPs, whose periodic response in the field enhancement disappears with tip lengthening due to increased losses. Furthermore, the single metal-dielectric interface at the apex means that any LSPs similar to those in MNPs have much weaker dipole moments and are therefore much

<sup>24</sup>Evaporation conditions used to roughly nanostructure a tip are similar to when depositing metal islands.

darker [127]. For realistic tip lengths all plasmon modes eventually disappear into a smooth, lightning rod continuum increasing into the IR [107].<sup>25</sup> As a result, smooth, sharp tips do not couple well with far-field light.

## Coupling with Metallic Substrates

An alternative strategy is to couple tips with a planar metallic substrate and form a plasmonic MIM cavity to better localise light [31, 103, 105, 119, 128–130]. In this instance, a weakly-excited dipole in the tip can induce an image dipole in the metallic surface to form a more strongly-confined coupled mode in the gap. Specifically, pairing a Au tip with a Au substrate greatly enhances the field localisation and strength, more so than when paired with a Pt surface [128] or a non-metallic surface [127]. This is attributed to better optical polarisability of the Au substrate. In these cases the Raman enhancement has been shown to rise to  $\sim 10^6\text{--}10^9$  [105]. Coupling can be achieved by either exciting the tip dipole or through SPP excitation on the underlying metallic substrate [103, 105]. Unlike the coupling between MNP plasmons, theory suggests that the coupling between a Au tip and a Au surface only minimally shifts the gap resonance ( $\Delta\lambda \sim 10\text{ nm}$ ), likely due to the reduced dipole moments in tips [127].

One final tip-based plasmon excitation mechanism of interest that has been discussed in recent years is electrical excitation. Similar to the use of EELS in electron microscopy, tunnelling electrons can be used to excite plasmons in an STM geometry. Since tips are typically illuminated with a single wavelength of light it becomes difficult to discern plasmonic features hidden in the collected light. Electrical excitation circumvents this limitation as electrons need only to have sufficient energy  $eV$  that a portion transferred to the conduction electrons is enough to excite SPs with frequencies  $\hbar\omega \leq eV$ . Electrical excitation also functions to both remove background light contributions to spectra by removing the illumination source.

Using tunnelling current excitation, light has been observed from both the tip-air-metal substrate gap [118, 119] and the interface between the metal substrate and its underlying dielectric [92]. Broad resonances, which redshift with decreasing tip-sample separation, are found superimposed onto TERS spectra when operating in the STM configuration [118, 119]. These suggest the formation of a MIM gap mode. Light detected from metal-glass interfaces is leakage radiation from SPPs on the metal-air interface. Since light cannot leak from SPPs at the metal-air interface the detected light must be scattering from gap plasmons between the tip apex and the surface. It is thought that 95% of the emission is due to SPP excitation rather than LSP excitation [92].



**Figure 1.21:** Comparison of TERS field enhancements and contrasts reported between 2000 and 2011 [89]. STM tips, likely due to their increased sharpness, outperform AFM tips. Ag tips outperform Au tips. Larger enhancements are observed in systems where there is an underlying thin, noble metallic film. Statistical correlations still remain somewhat weak, showing the current variability in TERS experiments, attributed to irreproducibility of enhancing tips.

### 1.3.2 Challenges associated with Tip Plasmonics

Since the initial measurements of tip enhancements and plasmons, techniques such as TERS and a-SNOM have become widespread. However, they are not currently reliable enough to be considered as a standard technique. Difficulty controlling the tip near-field is both a result of the irreproducibility of the tip geometry and a lack of understanding of the optical processes governing the enhancement, leading to large variations between reported field enhancements and TERS contrasts. A selection of these, reported between 2000 and 2011, are shown in Figure 1.21, showing the variability of TERS. The current challenges with TENOM are therefore improving the reproducibility of the near-field enhancement between tips [101, 102, 131] and achieving a better understanding of the tips themselves [107].

Factors determining the efficiency of TENOM include experimental excitation/collection geometry, tip sharpness, surface metal morphology, material influences and tip/apex orientation. From Figure 1.21 it is clear that sharper STM tips result in larger field enhancements than metallised AFM tips and comparative studies have shown similar trends [98, 132, 133]. Intuition suggests that the lightning rod effect must play a significant role in the near-field enhancement process. Theory showing drastic increases in the lightning rod effect after only small increases in sharpness (20 nm to 10 nm) gives some evidence towards this [107, 124], potentially explaining the varying measured field enhancements over time and between experiments. However, sharpness-induced enhancements can only be improved to a point as recent theory indicates the existence of a quantum limit set by nonlocal effects [134].<sup>26</sup> Understanding how to optimise the plasmonic component in tips is therefore a priority.

Materials choice, as with much of plasmonics, heavily influences any plasmonic behaviour. Ag tips generally outperform Au tips under visible light, although these claims highly depend on the underlying tip material and metal morphology. Only the metal and its morphology are important in solid STM tips and thickly metallised AFM tips, where plasmon energies are insensitive to any potential underlying materials. On thinly coated (< 40 nm) AFM tips, plasmons are tuned by the metal film thickness [116] and the refractive index of the underlying tip material. Tuning can vary drastically between materials such as Si, SiO<sub>2</sub>, and Si<sub>3</sub>N<sub>4</sub> [104, 133]. These high index materials can shift SPRs into the infrared and out of resonance with the pump laser frequency. Careful consideration must therefore be given when pairing a tip with a laser [98, 99, 121, 135].

A large amount of variability stems from surface metal morphology. Reliance on randomised apex geometries, as shown in Figure 1.20, for LSP excitation greatly limits reproducibility. Furthermore, this granularity is rarely taken into theoretical account when at-

---

<sup>25</sup>The apparent sharpness of the apex increases with wavelength as the field becomes larger relative to the apex curvature. Thus the lightning rod effect is greater at longer wavelengths [107].

<sup>26</sup>Field enhancement saturates as the potential around any finer structural imperfections becomes smoothed due to electron spill-out (non-locality).

tempting to explain TENOM. The orientation of the tip, along with the roughened apex, with respect to the sample and the incident excitation field is also known to influence near-field enhancement [98, 101].

Finally, variability between similar measurements can stem simply from differences in tip placement, optical setup, whether coupled with a mirror, and the specific illumination/collection geometry or optics used. As tips are rarely characterised there is little traceability between measurements from which to systematically determine the relevant causes for difference. It is highly likely, however, that geometrical limitations are the current dominating limitation restricting the progress of TENOM, leading to research into new tip geometries with better optimised, well-known optical responses.

### 1.3.3 Tip Modification, Nanostructuring and Optical Antenna Tips

The mode mismatch caused by the size difference between diffraction-limited light and the nanometre scale results in a 3–4 order of magnitude coupling efficiency loss [112]. As described previously, a SP acts as an optical antenna. A good optical antenna has the ability to effectively modify the local density of electromagnetic states such that the far-field, freely propagating optical radiation is efficiently converted into localised near-field evanescent modes and vice versa via intermediary plasmon states [25, 93]. Evidence suggests that sharp metallic tips, in their standard form, are not particularly good optical antennae, with most modes unresponsive to far-field light. To improve their coupling efficiency, standard sharp tips have been modified or nanostructured to introduce the necessary intermediary plasmon states [136]. Whilst previously achieved by roughening the metal surface, more reliable and reproducible methods have been developed in recent years to controllably nanostructure the tip and engineer the optical response.

Gratings imprinted onto the side of tips can transform the apex into a nanoscale, single wavelength light source as SPPs excited on the grating propagate to the apex and re-radiate on 10 nm length scales [137, 138].<sup>27</sup> Far-field illumination remains spatially separated from the apex, suppressing background scatter and allowing only near-field scattering from the apex to be measured, producing background-free TERS signals [23, 112].

Nanostructuring of the tip apex has been investigated in order to engineer and tune an optical antenna precisely at the apex. Tips are structured with distinct, sub-wavelength-sized metallic features in order to create the necessary antenna-like LSPs to enable far-field excitation in the visible region of the EM spectrum. Etching [139, 140], focussed ion beam (FIB) machining [141–143], selective deposition [144], MNP pickup [145], and nanostructure grafting [146] have all been successfully used to nanostructure optical antenna tips, though each process is complex and time consuming. Scattering resonances in the visible-NIR spectrum have

---

<sup>27</sup>Single wavelength operation results from adiabatic nanofocussing of only a single  $\lambda = 800$  nm mode.

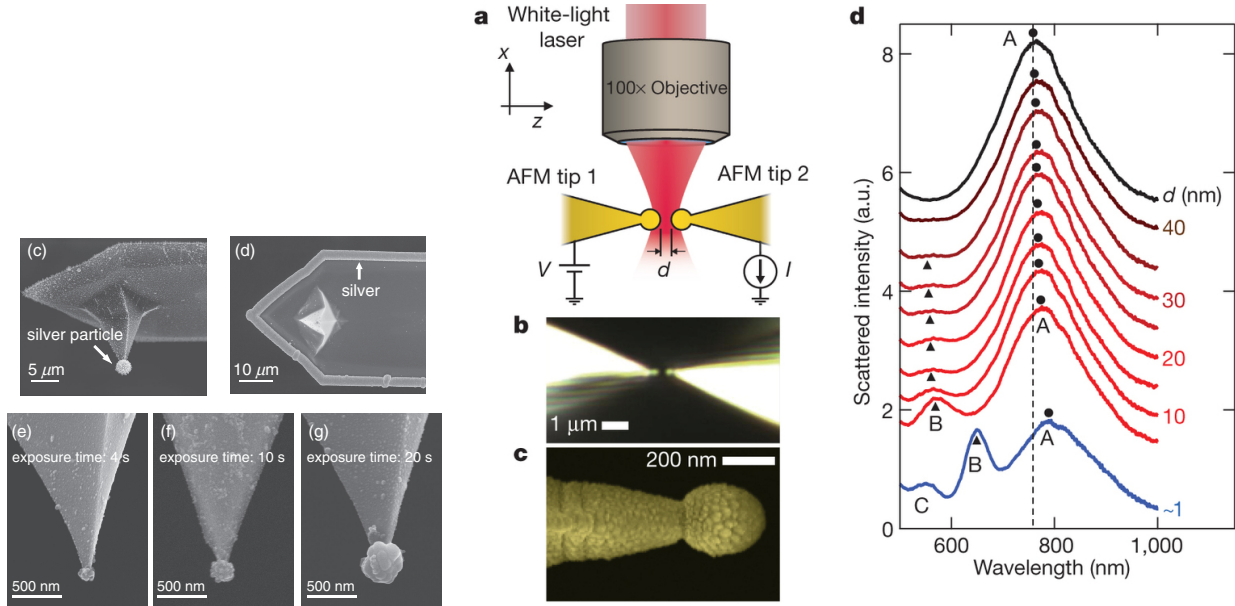


**Figure 1.22: Examples of spherical tip fabrication and surface plasmon resonances.** (left) Photochemically fabricated AgNP-on-Si tips for TERS [147]. Field enhancement is increased  $\sim 20\times$  compared with sharp Ag tips when using 488 nm illumination with a 1.4 NA objective in an inverted microscope. (right) Experimental evidence of LSPs in 50 nm Au-coated, 150 nm radius spherical AFM probes (NanoTools B150) [69]. The large radius minimises sensitivity to axial tip-tip alignment, increases scattered signal levels, and supports higher-order plasmonic cavity modes in the visible spectrum. Resonances are far-field excited using a supercontinuum laser source in a side-illumination configuration. Separation-dependent coupling between two spherical tips confirms plasmonic behaviour.

been directly measured on a subset of these [143, 144] while other reports use improvements in the field enhancement as a measurement of antenna quality [140, 146, 147]. In such cases the field enhancement can be improved by an order of magnitude through LSP excitation [141, 142, 147].

Lack of a strong plasmonic contribution from sharp Au metallised tips to TENOM is further evident from direct comparison with Au nanotip probes. A Si tip with the apex replaced by a Au nanocone outperforms a standard Au AFM tip by 120% in the side illumination geometry [146]. Similarly, cutting the Au coating off past the apex also enables LSPs [144]. Each of these modifications is carried out using FIB machining and is therefore highly controllable, though costly in time and resources.

The simplest geometry to impart onto a tip apex is a sub-wavelength metal sphere. By doing so the tip gains LSPs similar to those in an isolated spherical MNP. The specific SPRs depend on the sphere material and geometry along with the attachment method since the base tip structure determines the local adjacent dielectric medium. Coupled SPRs between two spherical Au tips have been previously observed in the far-field [69], but no characterisation has yet been done. Additionally, a  $20\times$  increase in field enhancement and spatial resolution

has been measured when using a photochemically-fabricated AgNP-on-Si tip compared with a sharp Ag tip [147]. These demonstrate that spherical metallic tips have the potential to improve TENOM if they can be fully understood.

To date there are very few reported methods of simply nanostructuring a tip without the need for FIB, electron microscopy or complex chemistry, justifying the study of how to produce good plasmonic tips. A simple approach for chemically producing plasmonic tips is explored and developed, specifically targeting the spherical tip apex geometry. Other than their successful application in TERS and fundamental plasmonics studies, the origin of LSPs in spherical tips has not yet been fully investigated. Very little work has been done to reliably produce, characterise and understand the optics of spherically nanostructured tips. Furthermore, there is still additional work needed to similarly investigate the optical response of sharp tips, comparing them directly with nanostructured tips in both fundamental studies and near-field enhancement applications.

## 1.4 Conclusions

The coupling of plasmons in metallic nanostructures is now widely exploited in order to enhance and confine optical fields on nanometric scales. In order to maximise enhancement, the characteristic scales of these gap structures is rapidly approaching the sub-nm level where quantum mechanics can no longer be ignored. As recent results have shown, charge transfer in such small gaps can lead to the emergence of new plasmonic phenomena and a break down of classical field confinement. This regime must therefore be well understood if the characteristic length scales of plasmonic devices are to continue decreasing.

The effects of electron tunnelling in sub-nm plasmonic gaps have only been touched upon in recent years and still requires significant investigation. To this extent, tips whose plasmons readily couple with light provide a useful platform for dynamically studying the fundamental plasmonics of nano-gaps. Their well-developed experimental geometries for topological measurements form the basis of microscopes integrating optics and tip-based surface techniques. By using such a setup, tunnelling plasmonics can be further investigated by controllably reducing a gap into the sub-nm regime.

To date there have been no direct correlated measurements between plasmon resonances and quantum transport effects. Tunnelling has been inferred from direct measurements of plasmon resonances without electronic measurements [69, 72] and from variables influenced by the gap field enhancement, which in some cases provide electronic measurements [66, 70, 71, 74]. The effects of quantum charge transport, specifically the relations between screening and CTP excitation, can be better understood with correlated electrical and force measurements. By using an experimental geometry related to AFM these measurements become possible.

# References

- [1] P. Drude, Annalen der Physik **306**, 566–613 (1900).
- [2] P. B. Johnson and R.-W. Christy, Physical Review B **6**, 4370 (1972).
- [3] R. Egerton, *Electron energy-loss spectroscopy in the electron microscope* (Springer Science & Business Media, 2011).
- [4] C. Kittel, P. McEuen, and P. McEuen, *Introduction to solid state physics*, Vol. 8 (Wiley New York, 1976).
- [5] A. Otto, Zeitschrift für Physik **216**, 398–410 (1968).
- [6] E. Kretschmann, Zeitschrift für Physik **241**, 313–324 (1971).
- [7] R. Wood, The London, Edinburgh, and Dublin Philosophical Magazine and Journal of Science **4**, 396–402 (1902).
- [8] U Fano, JOSA **31**, 213–222 (1941).
- [9] W. A. Murray and W. L. Barnes, Advanced materials **19**, 3771–3782 (2007).
- [10] S. A. Maier, *Plasmonics: fundamentals and applications* (Springer Science & Business Media, 2007).
- [11] J. D. Jackson, *Classical electrodynamics* (John Wiley & Sons, 1999).
- [12] E Prodan and P. Nordlander, The Journal of chemical physics **120**, 5444–5454 (2004).
- [13] C Sönnichsen et al., Applied Physics Letters **77**, 2949–2951 (2000).
- [14] J. Krenn et al., Applied Physics Letters **77**, 3379–3381 (2000).
- [15] J. Mock et al., The Journal of Chemical Physics **116**, 6755–6759 (2002).
- [16] H. Kuwata et al., Applied physics letters **83**, 4625–4627 (2003).
- [17] X. Huang et al., Journal of the American Chemical Society **128**, 2115–2120 (2006).
- [18] X. Huang et al., Lasers in medical science **23**, 217–228 (2008).
- [19] X. Huang and M. A. El-Sayed, Journal of Advanced Research **1**, 13–28 (2010).
- [20] C. Noguez, The Journal of Physical Chemistry C **111**, 3806–3819 (2007).
- [21] I. S. Grant and W. R. Phillips, *Electromagnetism* (John Wiley & Sons, 2013).
- [22] C. F. Bohren and D. R. Huffman, *Absorption and scattering of light by small particles* (John Wiley & Sons, 2008).
- [23] S. Berweger et al., The Journal of Physical Chemistry Letters **3**, 945–952 (2012).
- [24] P. Bharadwaj, B. Deutsch, and L. Novotny, Advances in Optics and Photonics **1**, 438–483 (2009).

- [25] L. Novotny and N. Van Hulst, *Nature Photonics* **5**, 83–90 (2011).
- [26] G. Mie, *Annalen der physik* **330**, 377–445 (1908).
- [27] F. Huang and J. J. Baumberg, *Nano letters* **10**, 1787–1792 (2010).
- [28] M. G. Millyard et al., *Applied Physics Letters* **100**, 073101 (2012).
- [29] J. Mertens et al., *Nano letters* **13**, 5033–5038 (2013).
- [30] R. W. Taylor et al., *Scientific reports* **4** (2014).
- [31] N. C. Lindquist et al., *Laser & Photonics Reviews* **7**, 453–477 (2013).
- [32] S. A. Maier, P. G. Kik, and H. A. Atwater, *Applied Physics Letters* **81**, 1714–1716 (2002).
- [33] T. Atay, J.-H. Song, and A. V. Nurmikko, *Nano Letters* **4**, 1627–1631 (2004).
- [34] O. Muskens et al., *Optics express* **15**, 17736–17746 (2007).
- [35] R. W. Taylor et al., *ACS nano* **5**, 3878–3887 (2011).
- [36] L. Herrmann et al., *Optics express* **21**, 32377–32385 (2013).
- [37] T. Okamoto and I. Yamaguchi, *The Journal of Physical Chemistry B* **107**, 10321–10324 (2003).
- [38] J. K. Daniels and G. Chumanov, *The Journal of Physical Chemistry B* **109**, 17936–17942 (2005).
- [39] M. K. Kinnan and G. Chumanov, *The Journal of Physical Chemistry C* **111**, 18010–18017 (2007).
- [40] S. Mubeen et al., *Nano letters* **12**, 2088–2094 (2012).
- [41] B. de Nijs et al., *Faraday Discussions* (2014).
- [42] I. Romero et al., *Optics Express* **14**, 9988–9999 (2006).
- [43] E. Hao and G. C. Schatz, *The Journal of chemical physics* **120**, 357–366 (2004).
- [44] C. E. Talley et al., *Nano Letters* **5**, 1569–1574 (2005).
- [45] U. Kreibig and M. Vollmer, *Optical properties of metal clusters*, Vol. 25 (Springer Berlin, 1995).
- [46] M. Gluodenis and C. A. Foss, *The Journal of Physical Chemistry B* **106**, 9484–9489 (2002).
- [47] W Rechberger et al., *Optics Communications* **220**, 137–141 (2003).
- [48] N. J. Halas et al., *Chemical reviews* **111**, 3913–3961 (2011).
- [49] P. K. Jain, W. Huang, and M. A. El-Sayed, *Nano Letters* **7**, 2080–2088 (2007).
- [50] X. Ben and H. S. Park, *The Journal of Physical Chemistry C* **115**, 15915–15926 (2011).
- [51] S. Kadkhodazadeh et al., *The Journal of Physical Chemistry C* **118**, 5478–5485 (2014).
- [52] P. Nordlander et al., *Nano Letters* **4**, 899–903 (2004).
- [53] E Prodan et al., *Science* **302**, 419–422 (2003).
- [54] P. Nordlander and E. Prodan, *Nano Letters* **4**, 2209–2213 (2004).

- [55] M.-W. Chu et al., *Nano letters* **9**, 399–404 (2008).
- [56] A. L. Koh et al., *Acs Nano* **3**, 3015–3022 (2009).
- [57] R. Esteban et al., *Nature Communications* **3**, 825 (2012).
- [58] J. B. Lassiter et al., *Nano letters* **8**, 1212–1218 (2008).
- [59] O Pérez-González et al., *Nano letters* **10**, 3090–3095 (2010).
- [60] O Pérez-González, N Zabala, and J Aizpurua, *New Journal of Physics* **13**, 083013 (2011).
- [61] C. Tserkezis et al., *Optics express* **22**, 23851–23860 (2014).
- [62] R. Esteban et al., *Faraday discussions* **178**, 151–183 (2015).
- [63] D. J. Griffiths, *Introduction to quantum mechanics* (Pearson Education India, 2005).
- [64] J. G. Simmons, *Journal of Applied Physics* **34**, 1793–1803 (1963).
- [65] J. M. Blanco, F. Flores, and R. Pérez, *Progress in surface science* **81**, 403–443 (2006).
- [66] S. F. Tan et al., *Science* **343**, 1496–1499 (2014).
- [67] J. Zuloaga, E. Prodan, and P. Nordlander, *Nano letters* **9**, 887–891 (2009).
- [68] R. Landauer, *IBM Journal of Research and Development* **1**, 223–231 (1957).
- [69] K. J. Savage et al., *Nature* **491**, 574–577 (2012).
- [70] H. Cha, J. H. Yoon, and S. Yoon, *ACS nano* **8**, 8554–8563 (2014).
- [71] W. Zhu and K. B. Crozier, *Nature communications* **5** (2014).
- [72] J. A. Scholl et al., *Nano letters* **13**, 564–569 (2013).
- [73] V. Kravtsov et al., *Nano letters* **14**, 5270–5275 (2014).
- [74] G. Hajisalem, M. S. Nezami, and R. Gordon, *Nano letters* **14**, 6651–6654 (2014).
- [75] M. Barbry et al., *Nano letters* (2015).
- [76] F. Benz et al., *Nano letters* **15**, 669–674 (2014).
- [77] L. O. Herrmann et al., *Nature communications* **5** (2014).
- [78] R. M. Stöckle et al., *Chemical Physics Letters* **318**, 131–136 (2000).
- [79] M. S. Anderson, *Applied Physics Letters* **76**, 3130–3132 (2000).
- [80] N. Hayazawa et al., *Optics Communications* **183**, 333–336 (2000).
- [81] B. Pettinger et al., *Electrochemistry* **68**, 942–949 (2000).
- [82] F Zenhausern, M. O’boyle, and H. Wickramasinghe, *Applied Physics Letters* **65**, 1623–1625 (1994).
- [83] F. Zenhausern, Y Martin, and H. Wickramasinghe, *Science* **269**, 1083–1085 (1995).
- [84] R Bachelot, P Gleyzes, and A. Boccara, *Optics letters* **20**, 1924–1926 (1995).
- [85] B Knoll et al., *Applied physics letters* **70**, 2667–2669 (1997).
- [86] B Knoll and F Keilmann, *Applied Physics A: Materials Science & Processing* **66**, 477–481 (1998).
- [87] F Keilmann, B Knoll, and A Kramer, *physica status solidi (b)* **215**, 849–854 (1999).

- [88] J. Wessel, *JOSA B* **2**, 1538–1541 (1985).
- [89] B. Pettinger et al., *Annual review of physical chemistry* **63**, 379–399 (2012).
- [90] C. Neacsu, G. Steudle, and M. Raschke, *Applied Physics B* **80**, 295–300 (2005).
- [91] D Mehtani et al., *Journal of Optics A: Pure and Applied Optics* **8**, S183 (2006).
- [92] T Wang et al., *Nanotechnology* **22**, 175201 (2011).
- [93] L. Novotny and S. J. Stranick, *Annu. Rev. Phys. Chem.* **57**, 303–331 (2006).
- [94] J. Steidtner and B. Pettinger, *Review of Scientific Instruments* **78**, 103104 (2007).
- [95] R Zhang et al., *Nature* **498**, 82–86 (2013).
- [96] H. K. Wickramasinghe et al., *ACS nano* **8**, 3421–3426 (2014).
- [97] N. Hayazawa et al., *Chemical Physics Letters* **335**, 369–374 (2001).
- [98] B.-S. Yeo et al., *Applied spectroscopy* **60**, 1142–1147 (2006).
- [99] B.-S. Yeo et al., *Analytical and bioanalytical chemistry* **387**, 2655–2662 (2007).
- [100] M. Zhang et al., *Journal of Optics* **15**, 055006 (2013).
- [101] T. Mino, Y. Saito, and P. Verma, *ACS nano* **8**, 10187–10195 (2014).
- [102] N. Kumar, A. Rae, and D. Roy, *Applied Physics Letters* **104**, 123106 (2014).
- [103] N. Hayazawa et al., *Japanese Journal of Applied Physics* **46**, 7995 (2007).
- [104] A. Taguchi et al., *Optics express* **17**, 6509–6518 (2009).
- [105] K. Uetsuki et al., *Nanoscale* **4**, 5931–5935 (2012).
- [106] R Esteban, R Vogelgesang, and K Kern, *Nanotechnology* **17**, 475 (2006).
- [107] W. Zhang, X. Cui, and O. J. Martin, *Journal of Raman Spectroscopy* **40**, 1338–1342 (2009).
- [108] T. Schmid et al., *Angewandte Chemie International Edition* **52**, 5940–5954 (2013).
- [109] M Zhang, J Wang, and Q Tian, *Optics Communications* **315**, 164–167 (2014).
- [110] M. I. Stockman, *Physical review letters* **93**, 137404 (2004).
- [111] D. Pile and D. K. Gramotnev, *Applied Physics Letters* **89**, 041111 (2006).
- [112] S. Berweger et al., *The Journal of Physical Chemistry Letters* **1**, 3427–3432 (2010).
- [113] J. S. Lee et al., *Optics express* **19**, 12342–12347 (2011).
- [114] R. M. Roth et al., *Optics Express* **14**, 2921–2931 (2006).
- [115] A. Goncharenko et al., *Applied physics letters* **88**, 104101 (2006).
- [116] C. Huber et al., *Physical Chemistry Chemical Physics* **16**, 2289–2296 (2014).
- [117] C. A. Barrios et al., *The Journal of Physical Chemistry C* **113**, 8158–8161 (2009).
- [118] B. Pettinger et al., *Physical Review B* **76**, 113409 (2007).
- [119] B. Pettinger et al., *Surface Science* **603**, 1335–1341 (2009).
- [120] E. Bailo and V. Deckert, *Chemical Society Reviews* **37**, 921–930 (2008).
- [121] N. Hayazawa, T.-a. Yano, and S. Kawata, *Journal of Raman Spectroscopy* **43**, 1177–1182 (2012).

- [122] M. Fleischmann, P. J. Hendra, and A. McQuillan, *Chemical Physics Letters* **26**, 163–166 (1974).
- [123] D. L. Jeanmaire and R. P. Van Duyne, *Journal of Electroanalytical Chemistry and Interfacial Electrochemistry* **84**, 1–20 (1977).
- [124] L. Meng et al., *Optics Express* **23**, 13804–13813 (2015).
- [125] C. Schäfer et al., *Nanoscale* **5**, 7861–7866 (2013).
- [126] S. Cherukulappurath et al., *Nano letters* **13**, 5635–5641 (2013).
- [127] A. Downes, D. Salter, and A. Elfick, *The Journal of Physical Chemistry B* **110**, 6692–6698 (2006).
- [128] B. Ren, G. Picardi, and B. Pettinger, *Review of Scientific Instruments* **75**, 837–841 (2004).
- [129] C. C. Neacsu et al., *Physical Review B* **73**, 193406 (2006).
- [130] T.-a. Yano et al., *Applied Physics Letters* **91**, 121101 (2007).
- [131] C. Blum et al., *Journal of Raman Spectroscopy* **45**, 22–31 (2014).
- [132] M. B. Raschke and C. Lienau, *Applied Physics Letters* **83**, 5089–5091 (2003).
- [133] G. Picardi et al., *The European Physical Journal Applied Physics* **40**, 197–201 (2007).
- [134] A. Wiener et al., *Nano letters* **12**, 3308–3314 (2012).
- [135] X. Cui et al., *Optics express* **15**, 8309–8316 (2007).
- [136] N. Mauser and A. Hartschuh, *Chemical Society reviews* **43**, 1248–1262 (2014).
- [137] C Ropers et al., *Nano letters* **7**, 2784–2788 (2007).
- [138] C. C. Neacsu et al., *Nano letters* **10**, 592–596 (2010).
- [139] P. Uebel et al., *Applied Physics Letters* **103**, 021101 (2013).
- [140] S. Kharintsev et al., *Journal of Physics D: Applied Physics* **46**, 145501 (2013).
- [141] A Weber-Bargioni et al., *Nanotechnology* **21**, 065306 (2010).
- [142] M. Fleischer et al., *ACS nano* **5**, 2570–2579 (2011).
- [143] I. Maouli et al., *Applied Physics Express* **8**, 032401 (2015).
- [144] Y. Zou et al., *Applied Physics Letters* **94**, 171107 (2009).
- [145] A. I. Denisyuk et al., *Journal of nanoscience and nanotechnology* **12**, 8651–8655 (2012).
- [146] F. Huth et al., *Nano letters* **13**, 1065–1072 (2013).
- [147] T. Umakoshi et al., *Applied Physics Express* **5**, 052001 (2012).